

The *Spitzer* mid-infrared AGN survey. I - optical and near-infrared spectroscopy of candidate obscured and normal AGN selected in the mid-infrared.

M. Lacy¹, S.E. Ridgway², E.L. Gates³, D.M. Nielsen⁴, A.O. Petric⁵, A. Sajina⁶, T. Urrutia⁷, S. Cox-Drews⁸, C. Harrison⁹, N. Seymour¹⁰, L.J. Storrie-Lombardi¹¹

ABSTRACT

We present the results of a program of optical and near-infrared spectroscopic follow-up of candidate Active Galactic Nuclei (AGN) selected in the mid-infrared. This survey selects both normal and obscured AGN closely matched in luminosity across a wide range, from Seyfert galaxies with bolometric luminosities $L_{\text{bol}} \sim 10^{10} L_{\odot}$, to highly luminous quasars ($L_{\text{bol}} \sim 10^{14} L_{\odot}$), and with redshifts from 0-4.3. Samples of candidate AGN were selected through mid-infrared color cuts at several different $24\mu\text{m}$ flux density limits to ensure a range of luminosities at a given redshift. The survey consists of 786 candidate AGN and quasars, of which 672 have spectroscopic redshifts and classifications. Of these, 137 (20%) are type-1 AGN with blue continua, 294 (44%) are type-2 objects with extinctions $A_V \gtrsim 5$ towards their AGN, 96 (14%) are AGN with lower extinctions ($A_V \sim 1$) and 145 (22%) have redshifts, but no clear signs of AGN activity in their spectra. 50% of the survey objects have $L_{\text{bol}} > 10^{12} L_{\odot}$, in the quasar regime. We present composite spectra for type-2 quasars and for objects with no signs of AGN activity in their spectra. We also discuss the mid-infrared – emission-line luminosity correlation and present the results of cross-correlations with serendipitous X-ray and radio sources. The results show that: (1) obscured objects dominate the overall AGN population, (2) there exist mid-infrared selected AGN candidates which lack AGN signatures in their optical spectra, but have AGN-like X-ray or radio counterparts, and (3) X-ray and optical classifications of obscured and unobscured AGN often differ.

Subject headings: quasars:general – galaxies:Seyfert – infrared:galaxies – galaxies:starburst

¹National Radio Astronomy Observatory, 520 Edgemont Road, Charlottesville, Virginia 22903

²National Optical Astronomy Observatory, 950 North Cherry Avenue, Tucson, AZ 85719

³UCO/Lick Observatory, P.O. Box 85, Mount Hamilton, CA 95140

⁴Department of Astronomy, University of Wisconsin, 475 N. Charter Street, Madison, WI 53706

⁵Department of Astronomy, California Institute of Technology, Pasadena, CA 91125

⁶Department of Physics and Astronomy, Tufts University, 212 College Avenue, Medford, MA 02155

⁷Leibniz-Institut für Astrophysik Potsdam, An der Sternwarte 16, 14482, Potsdam, Germany

⁸946 Mangrove Avenue #102, Sunnyvale, CA 94086

⁹Department of Astronomy, University of Michigan, Ann Arbor, MI 48109

¹⁰CSIRO, P.O. Box 76, Epping, NSW 1710, Australia

1. Introduction

The past decade has seen a dramatic improvement in our ability to find AGN that would be missing, or strongly selected against, in samples based on selection in the optical. There are several reasons why finding these objects is of interest. First, the fraction of AGN obscured by dust represents a significant uncertainty in studies of AGN evolution. Second, the total number of AGN (obscured plus unobscured) is needed to estimate the mean efficiency of black hole accretion using the Soltan (1982) argument (Martinez-Sansigre & Taylor 2009). Third, some obscured AGN may represent an early phase in AGN activity, as predicted by several models, and finding them would confirm the importance of merger-driven evolution of massive galaxies, and give strong clues about the nature of AGN feedback. Fourth, a sample of luminous AGN without a bright point source nucleus makes host galaxy studies of large numbers of these objects feasible.

Until the Sloan Digital Sky Survey (SDSS) and *Spitzer*, only a handful of high luminosity obscured AGN that were not either radio-loud (i.e. radio galaxies), or low luminosity (i.e. Seyfert-2 galaxies, rather than objects of quasar-like luminosity) were known. Norman et al. (2002) found an example radio-quiet type-2 quasar in the Chandra Deep Field South (CDFs), but the small areas of X-ray surveys mean that relatively few high luminosity objects have been discovered in them. Radio-loud examples of this dusty type-1 quasar population had been identified by Webster et al. (1998), but the degree to which synchrotron emission from jets associated with the radio source dominated the optical emission was unclear (Whiting et al. 2001). Using the 2-Micron All-Sky Survey (2MASS)

and near-infrared color selection, Cutri et al. (2001) were able to identify over 200 $z \sim 0.2$ radio-quiet red AGN, most likely reddened by dust (a similar technique, but using *Spitzer* $8\mu\text{m}$ photometry as the long wavelength data point, was used by Brown et al. 2006). Gregg et al. (2002) used a combination of 2MASS and radio emission in the Faint Images of the Radio Sky at Twenty-cm (FIRST) survey to improve the reliability of selection of red quasars by excluding non-AGN. These techniques typically found less heavily obscured AGN ($A_V \sim 1 - 3$), predominantly broad-lined objects. This population of lightly dust-reddened AGN was found to contribute significantly ($\sim 20\%$) to the overall AGN population at quasar-like luminosities, and has properties consistent with an early phase in quasar evolution (Lacy et al. 2002; Glikman et al. 2004, 2007; Urrutia et al. 2009, 2012). All of these early techniques, however, were still biased against true “type-2” AGN with rest-frame $A_V \gtrsim 10$.

Narrow-line selection of type-2 AGN from the Sloan Digital Sky Survey (SDSS) (Zakamska et al. 2003; Reyes et al. 2008) increased sample sizes of obscured, high luminosity AGN to several hundred at $z < 0.8$, where the [OIII]5007 line is visible in the optical. Mid-infrared selection of obscured AGN using *Spitzer* colors was then developed by Lacy et al. (2004), Sajina, Lacy & Scott (2005) and Stern et al. (2005). In parallel, several other groups were working on joint radio/mid-infrared selection (Martinez-Sansigre et al. 2005, Donley et al. 2005 and Park et al. 2008), which gave more reliable, but less complete samples, missing radio-quiet objects. Mid-infrared techniques have found a significant population of both reddened type-1 and luminous type-2 AGN at $z > 1$ (e.g. Lacy et al. 2007a; hereafter L07), including the discovery of heavily absorbed objects invisible in all but the deepest X-ray surveys.

¹¹Spitzer Science Center, California Institute of Technology, Pasadena, CA91125

Mid-infrared selected samples are not immune to problems; in particular they do not discriminate in principle between dust heated by an extremely dense, hot starburst, and an AGN power source (so reliable samples require spectroscopic follow-up, as detailed in this paper), and the technique is not effective at finding AGN which lack a hot dust component, such as low accretion rate radio galaxies (e.g. Ogle et al. 2006). However, these samples do seem to be complete for rapidly accreting, luminous AGN.

Using these early mid-infrared samples containing $\sim 10 - 100$ objects, Martínez-Sansigre et al. (2005) and L07 were able to show that dust-obscured AGN are at least as common as “normal” blue AGN, even at high luminosities. These conclusions were also reached by Reyes et al. (2008) using SDSS optical selection of type-2s, with a much larger sample (887 objects) at $z < 0.8$. These samples were, however, too restricted to examine trends of obscured AGN fraction as a function of both redshift and luminosity. Furthermore, the high redshift objects in the infrared-selected samples are, in general, significantly more luminous than those in X-ray samples of high redshift AGN, which are selected from relatively small fields (tens of square arcminutes, compared to tens of square degrees). In these less luminous AGN, *Hubble Space Telescope* images tend to reveal little disturbance in the host, even at high redshifts (Kocevski et al. 2012), in contrast, the majority of dust reddened quasars tend to have host galaxies showing strong signs of disturbance (Lacy et al. 2007b; Urrutia et al. 2008). There thus may be a difference in the physical causes of AGN activity in Seyfert-like objects, powered by secular processes or minor interaction/merger activity in individual galaxies, and quasars, powered by major galaxy-galaxy mergers (e.g. Treister et al. 2012).

We thus undertook a project to use the

wide-area *Spitzer* Wide-area Infrared Extragalactic survey (SWIRE; Lonsdale et al. 2003), the *Spitzer* Extragalactic First Look Survey (XFLS; Lacy et al. 2005; Fadda et al. 2006) and the *Spitzer* Cosmic Evolution Survey (SCOSMOS; Sanders et al. 2007) surveys to search for luminous AGN in an area of sky totaling 54 deg^2 , large enough to find examples of highly-luminous quasars at high redshifts. Furthermore, we nested our survey in terms of flux density limits at $24\mu\text{m}$ to ensure a good dynamic range in luminosity at a given redshift without the need to take many thousands of spectra. In this paper we present optical and near-infrared spectroscopy of our new survey. Our paper is structured as follows: Section 2 describes the selection of objects in the survey, how the individual sample flux limits were chosen to ensure a wide range in AGN luminosity at a given redshift, and what selection effects remain. Section 3 describes the spectroscopic observations, Section 4 describes the classification of the objects, Section 5, the X-ray detections in the survey, Section 6, the radio detections, Section 7, the objects lacking AGN signatures in the optical, Section 8, the mid-infrared – emission line luminosity correlation and Section 9 the composite spectra. Future papers (Ridgway et al. 2013; Lacy et al. 2013) will discuss the evolution and luminosity dependence of the demographics of the obscured AGN population, and the spectral energy distributions (SEDs) of the AGN.

For the purposes of this paper, we define a quasar as an AGN having a total accretion luminosity of $> 10^{12} L_{\odot}$ ($3.8 \times 10^{45} \text{ ergs}^{-1} \text{ cm}^{-2}$), which, assuming a bolometric correction to $15\mu\text{m}$ of nine from Richards et al. (2006) for both obscured and unobscured objects, corresponds to $\log_{10}(L_{15\mu\text{m}}[\text{ergs}^{-1} \text{ Hz}^{-1}]) > 31.3$, or $\log_{10}(\nu L_{15\mu\text{m}}[\text{ergs}^{-1}]) > 44.6$. (Note that this also corresponds approximately to $M_B(\text{Vega}) < -23.0$ for an unreddened

AGN.) We assume a cosmology with $H_0 = 70\text{kms}^{-1}\text{Mpc}^{-1}$, $\Omega_M = 0.3$ and $\Omega_\Lambda = 0.7$.

2. Survey selection

2.1. Infrared color selection criteria

The candidate AGN were selected from the XFLS, SWIRE and SCOSMOS fields. Several samples were selected limited at different $24\mu\text{m}$ flux density ranges to ensure a good spread of mid-infrared luminosities at a given redshift to aid with disentangling correlations due to redshift from those due to luminosity. Color selection based on the [3.6],[4.5], [5.8] and [8.0] flux densities from the Infrared Array Camera (IRAC) was then applied to each sample (Figure 1) in order to filter out low- z starbursts and quiescent galaxies as detailed in L07 (except with a slightly expanded region in color space allowed for the fainter $24\mu\text{m}$ samples, as discussed below).

The L07 color “wedge” selection is as follows:

$$\begin{aligned} \log_{10}(S_{8.0}/S_{4.5}) &\leq 0.8\log_{10}(S_{5.8}/S_{3.6}) + 0.5 \\ \&\log_{10}(S_{5.8}/S_{3.6}) &> -0.1 \\ \&\log_{10}(S_{8.0}/S_{4.5}) &> -0.2 \end{aligned} \tag{1}$$

the expanded selection is:

$$\begin{aligned} \log_{10}(S_{8.0}/S_{4.5}) &\leq 0.8\log_{10}(S_{5.8}/S_{3.6}) + 0.5 \\ \&\log_{10}(S_{5.8}/S_{3.6}) &> -0.3 \\ \&\log_{10}(S_{8.0}/S_{4.5}) &> -0.3 \end{aligned} \tag{2}$$

The samples are detailed in Table 1. Bright samples (those with flux density limits at $24\mu\text{m}$ ranging from $S_{24} > 4\text{mJy}$ to $> 10\text{mJy}$) were selected across all 54 deg^2 of the SWIRE fields, XFLS and SCOSMOS fields in order to maximize the volume probed for very luminous objects. Faint samples, with limits ranging from $S_{24} > 0.6$ to $> 1.2\text{mJy}$, were

selected in small areas in individual SWIRE fields (totalling 2.2 deg^2) to provide a range in luminosity at every redshift. In addition, we selected a sample with a very narrow range in S_{24} ($1.0 \leq S_{24} < 1.1\text{mJy}$) split between three separate fields, which we followed up with Gemini Multi-Object Spectrograph on Gemini South (GMOS-S) to improve our overall spectroscopic completeness at faint S_{24} (the “GMOSS” sample in Table 1). Altogether, our original selection included 963 candidate AGN (listed in Table 2), this was reduced by constraints on fiber placement to 786 objects for which spectroscopy was attempted, or had spectroscopic redshifts and type information in the literature (Table 3).

The selection region was changed from the L07 wedge (Eqn. 1) to Eqn. (2) for the fainter samples to improve our completeness in low luminosity AGN, which tend to have bluer colors as starlight dominates the spectral energy distribution (SED) at rest wavelengths $\sim 2 - 4\mu\text{m}$ rather than AGN dust emission. The expanded criteria were determined by taking the SEDs of several well-studied type-2 quasars from Lacy et al. (2007b) and changing the redshifts and relative contributions of the AGN components. This resulted in the trajectories in color space shown in Figure 1, and led us to the conclusion that, to increase completeness, we needed to expand the wedge. Expanding the wedge in this way inevitably results in more contamination, but the spectroscopy is able to remove the objects more likely to be starbursts from the final AGN sample.

Figure 2 shows the actual objects, color coded according to type (see Section 4.2), in the selection region. In general, the AGN of all types lie close to the locus formed by the type-1s, however, many of the type-2s scatter above this line, presumably due to the presence of polycyclic aromatic hydrocarbon (PAH) emission in the mid-IR spectra. There

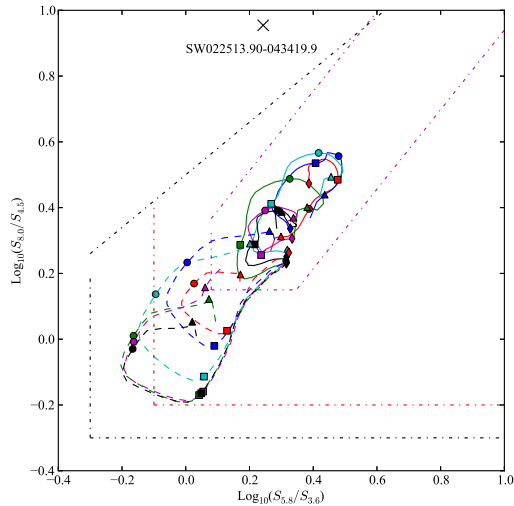


Fig. 1.— Trajectories of six $z \sim 0.6$ type-2 quasars (from Lacy et al. 2007b, selected to have $S_{[8.0]} > 1\text{mJy}$) in color-color space. Solid lines represent the unmodified fits to the SEDs, dashed lines the same objects, but with the AGN mid-infrared component reduced by a factor of ten to represent objects close to the limit of our faintest samples. Symbols represent redshifts of 0.3 (triangles), 1.0 (circles), 2.0 (squares) and 5.0 (diamonds). The red dot-dash line represents the L07 criteria, the black dot-dash line the expanded wedge used for the faint samples, and the magenta dot-dash line the AGN selection criteria of Donley et al. (2012). The black cross near the top of the plot marks the position of SW022513.90-043419.9, a $z = 3.43$ type-2 quasar discovered by Polletta et al. (2008) (see Section 6 for discussion).

is also a trend for high redshift objects to have redder colors in general. Note that the expanded wedge selection did indeed make us more complete to low luminosity type-2s, though the overall reliability was relatively low within the expansion region - of 94 extragalactic objects which lie only in the expanded region, 51 (54%) have non-AGN optical spectra, nine (10%) have featureless spectra and 34 (36%) have AGN spectra.

Various criteria for the mid-infrared color selection of AGN are compared and discussed in detail in Donley et al. (2012). They show that it is possible to come up with better optimized selection for AGN using IRAC colors, especially with regards to increased reliability of AGN selection. As Figure 2 shows, though, the strictness of the Donley et al. (2012) criteria does result in a significant fraction of AGN being missed, particularly type-2s.

2.2. Biases and incompleteness

We know of several selection effects that will remove objects from these samples. In general, mid-infrared selection does not work well for objects with low accretion rates ($\lesssim 0.01$ Eddington, e.g. low luminosity radio galaxies [Ogle et al. 2006] and LINERS [Sturm et al. 2006]), whose mid-infrared luminosities are low compared to their bolometric output, perhaps because they lack the torus structure of objects that accrete at a higher rate, and which is thought to be responsible for the mid-infrared emission from AGN.

A second source of incompleteness was discussed in L07. It occurs at $z < 0.3$, when the $7.7\mu\text{m}$ PAH feature from star formation is present in the IRAC $8.0\mu\text{m}$ band, and can be of high enough equivalent width that the $S_{8.0}/S_{4.5}$ ratio is too high for the object to be classed as an AGN. Objects for which this occurs are typically low luminosity objects, with weak mid-infrared continua, as, for a given amount of PAH luminosity, the equiv-

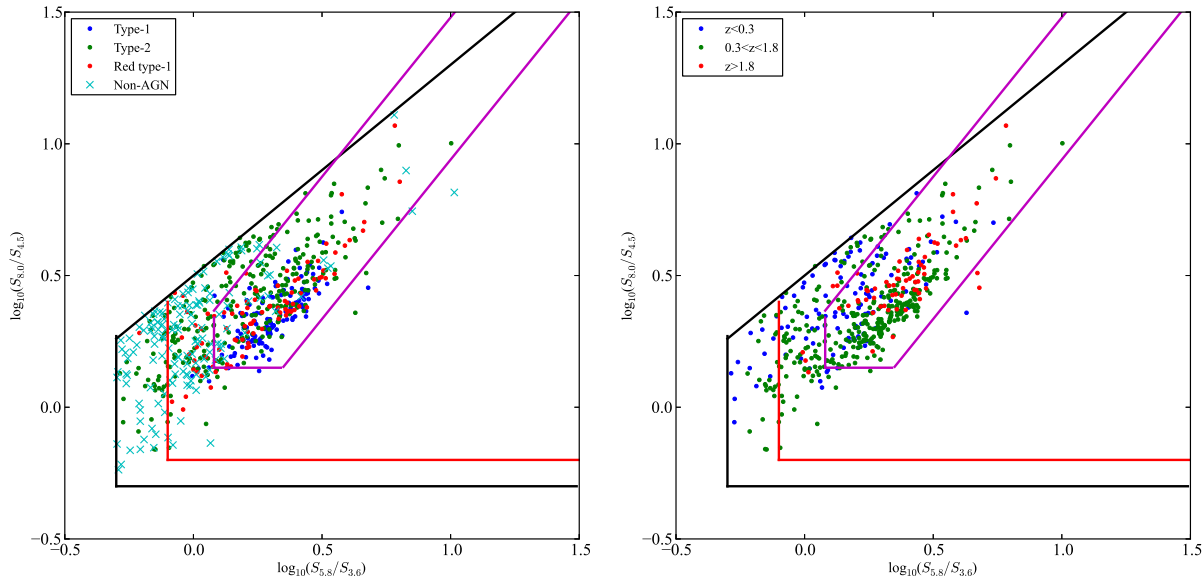


Fig. 2.— Objects, colored according to (a) type (for all objects), and (b) redshift (for confirmed AGN only). The selection for the “expanded” wedge, used for the faint samples, is shown as the black solid line. The selection of L07, used for the brighter samples, is shown as the red solid line. The selection criteria of Donley et al. (2012) is shown as the magenta solid line. Note that the Donley et al. criteria also require a monotonic increase in flux from [3.6] through [8.0].

alent width of the feature will be higher if the continuum is weak, however, our overall completeness is significantly compromised at those redshifts (by perhaps as much as 50% based on L07). The effects of this on our estimate of the AGN luminosity function will be discussed in Ridgway et al. (2013).

A third possible selection effect is related to the highest redshift objects only, where the colors become more difficult to predict, and the requirement for four-band IRAC detection means that some extreme objects may be missed. Although we have succeeded in finding several high redshift objects, both of the $z \sim 3.5$ objects of Polletta et al. (2008) would have been missed from the color selection due to their very steep mid-infrared spectra at $> 5\mu\text{m}$ in the observed frame (indeed, one of them, SW0225550.32-042149.6, is not even detected at $5.8\mu\text{m}$ in SWIRE). Objects with extremely low ratios of stellar host luminosity to AGN hot dust luminosity are not represented in our models in Figure 1 (or in Sajina et al. 2005), but seem to be present at high redshift. The redshift range $z \sim 3 - 4$ is likely to be particularly problematic, as

the $5.8\mu\text{m}/3.6\mu\text{m}$ (rest frame $\sim 1.3\mu\text{m}/0.8\mu\text{m}$) color is dominated by stellar emission from the host, with only a small contribution from the AGN power-law, and is thus relatively blue, whereas the $8.0\mu\text{m}/4.5\mu\text{m}$ (rest-frame $1.8\mu\text{m}/1.0\mu\text{m}$) color can be very red if the AGN is powerful and dominates the $8.0\mu\text{m}$ flux, as the $4.5\mu\text{m}$ emission will be dominated by stellar emission from the host. At $z < 3$, the effect will be less pronounced. The $5.8\mu\text{m}/3.6\mu\text{m}$ will be redder because more of the AGN emission is in the $5.8\mu\text{m}$ band, and the object will move into the selection wedge (to the right in Figure 1). Similarly, at $z > 4$, the $8.0\mu\text{m}$ emission from the AGN will be more diluted by the stellar population of the host, rendering the $8.0\mu\text{m}/4.5\mu\text{m}$ color bluer, moving the object down into the selection wedge in Figure 1. A related source of bias against high redshift objects is that high redshift objects with very faint host galaxies would have been missed at the shorter wavelengths, where the host galaxy dominates the SED.

We can quantify some of these incompleteness effects with the aid of the new *Spitzer*

Extragalactic Representative Volume Survey (SERVS; Mauduit et al. 2012), which provides deep IRAC 3.6 and $4.5\mu\text{m}$ data over a total of 18 deg^2 spread over several SWIRE fields. First, we examined how many reddened, high redshift AGN we may be missing due to their falling outside of our selection wedge (e.g. SW022513.90-043419.9 in Figure 1). In the 4 deg^2 Lockman Hole SERVS field, we find 38 objects with $S_{24} > 1\text{mJy}$ (comparable to our “Deep” sample flux limits) that have $\log_{10}(S_{5.8}/S_{3.6}) > 0.1$ and lie above the diagonal line in Figure 1 (and therefore are candidates for very high redshift objects missed by our selection wedge). Only 13 of these, however, have $r > 20$, consistent with them being $z > 0.3$ objects missed by our selection. The “Deep” fields in this paper contain 405 objects (with 90% redshift completeness) within a comparable area (3.2deg^2). The addition of ~ 10 more high redshift objects would thus not severely affect the completeness of the sample, though losing these may lead to a bias against the highest redshift obscured quasars. Second, we examine how many objects may be missing due to not being detected in the shortest wavelength IRAC bands given the SWIRE and XFLS flux density limits. By combining with SERVS 3.6 and $4.5\mu\text{m}$ data, we were able to verify that the faintest object at $3.6\mu\text{m}$, with $S_{3.6} = 8\mu\text{Jy}$, is above the flux density limit of SWIRE ($S_{3.6} = 7.3\mu\text{Jy}$), though below that of the XFLS ($S_{3.6} = 20\mu\text{Jy}$). Given the density of sources with $S_{3.6} < 20\mu\text{Jy}$, we estimate that four objects may be missing from our XFLSDeep sample.

3. Observations

3.1. Optical spectroscopy

A wide range of optical facilities and instruments were used for spectroscopic follow-up of our AGN candidates. Most of the bright samples were followed up with 3-5m tele-

scopes and longslit spectroscopy (Hale with COSMIC, SOAR with Goodman, Shane with Kast), whereas the fainter samples were followed up with multifiber and/or 6-8m class telescopes (Blanco with Hydra, MMT with Hectospec and Gemini-South with GMOS [program GS-2008B-C4]). We also obtained spectra of some of the bright candidates with a successful poor weather (scheduling band 4) program at Gemini-South (program GS-2008B-Q86). Some objects had spectra available in archives from the SDSS, 2dF (Colless et al. 2001) or 6dF (Jones et al. 2009) surveys, and some have redshifts and classifications in the literature, all found using the NASA Extragalactic Database (NED). Table 2 (full table in electronic format) gives details of the spectroscopic observations or literature references as appropriate. Note that we include the previously-published spectra of L07 for completeness. (For reasons of space the optical spectra are not shown in this paper, however, we intend to make them available electronically, either by direct application to the author, or through a data service.)

Data analysis followed standard procedures. Most of the data were analysed in IRAF, using the twodspec package to apply bias subtraction, flat fielding, wavelength calibration and extraction. Correction for atmospheric extinction was performed using mean extinction curves appropriate to the observatory. No correction has been made to the spectra for Galactic extinction.

The fiber data from the Hydra instrument was analysed in the hydra package of IRAF, with improved sky subtraction using our implementation of an algorithm used at the Anglo-Australian Telescope. This involved median filtering each fiber spectrum with a broad (201 pixel, 168\AA) filter, subtracting the median filtered continuum, then measuring the flux in the prominent sky lines at 5577\AA , 5892\AA , 6300\AA , 6363\AA and 6832\AA . The fluxes of the

same lines in the combined sky spectrum were then matched to these, and a mean scaling factor found, which was then applied to the sky spectrum before it was subtracted from the object spectrum.

The MMT Hectospec data were analysed using software based on the HSRED package of R. Cool, with the same modification discussed above to improve the sky subtraction. In most cases our sky subtraction technique works well, particularly for the discrete sky lines. Remnant sky lines were masked out in the final spectra. Fiber spectra of faint objects are, however, more vulnerable to artifacts due to poor sky subtraction than longslit spectra. In cases of low signal-to-noise, we therefore attempted to obtain confirmation via near-infrared spectroscopy (Section 3.1), or used SED fitting to check that the redshifts we obtained were consistent with the photometry (see Lacy et al. 2013).

In the case of the fiber spectrographs, $\approx 20\%$ of the candidates did not have spectra taken as we only used a single fiber configuration for each field. In some cases fibers could not be placed close enough together to obtain spectra for all objects (the minimum fibre separation was 20 arcseconds for Hectospec and 25 arcseconds for Hydra), in others objects were not observed in order to prevent fibers crossing. For these fields, the effective area was calculated as the area of the survey multiplied by the ratio of the number of objects for which spectra were attempted plus those which had spectra in the literature (and were therefore excluded from the fiber assignments) to the total number of candidates in the area and flux range. Exclusions due to fiber crowding were randomly determined to avoid possible bias.

3.2. Near-infrared spectroscopy

For some high redshift candidates with ambiguous or low signal-to-noise optical spectra

Table 1: Samples used

Name	Field center(s)	S_{24} range (mJy)	Effective area (sr)	N^a	selection	follow-up	completeness ($q^c \leq 3$)(%)	90% flux limit	N_{90}^b
ELAIS-S1Deep ^d	003444-4328	$1.30 \leq S_{24} < 5.8$	0.000103	27	Exp. wedge	CTIO/Hydra	15	2.98	4
ELAIS-S1Bright ^d	003830-4400	$S_{24} \geq 5.8$	0.002071	37	Exp. wedge	SOAR/Goodman; Gemini/GMOS	100	6.1	36
XMM-LSSBright ^d	022120-0430	$S_{24} \geq 6.6$	0.002772	34	L07 wedge	Hale/COSMIC	100	6.6	34
XMM-LSSDeep ^d	021910-0500	$1.19 \leq S_{24} < 6.6$	0.0000879	52	Exp. wedge	CTIO/Hydra	33	2.35	17
GDFSBright ^d	033200-2816	$S_{24} \geq 6.0$	0.002376	40	L07 wedge	SOAR/Goodman; Gemini/GMOS	100	6.0	40
GMOS-S ^d	003254-4253, 003444-4328, 021910-0500	$1.0 \leq S_{24} < 1.10$	0.000318	36	Exp. wedge	Gemini-S/GMOS; CTIO/Hydra	81	N/A	N/A
SCOSMOSBright ^e	100000+0200	$S_{24} \geq 6.3$	0.0006092	8	L07 wedge	SOAR	100	6.3	8
LockmanBright ^d	104500+5800	$S_{24} \geq 8.0$	0.003351	28	L07 wedge	Hale/COSMIC	96	8.0	27
LockmanDeep ^d	105248+5730	$1.0 \leq S_{24} < 8.0$	0.0002175	133	Exp. wedge	MMT/Hectospec	90	1.03	116
ELAIS-N1Deep ^d	161024+5436	$1.0 \geq S_{24} < 8.0$	0.0002132	132	Exp. wedge	MMT/Hectospec	86	1.306	76
ELAIS-N1Bright ^d	161100+5500	$S_{24} \geq 8.0$	0.002815	19	L07 wedge	Lick/Kast	88	9.6	13
ELAIS-N2Bright ^d	163648+4102	$S_{24} \geq 8.0$	0.001277	15	L07 wedge	Lick/Kast	100	8.0	15
XFLSBright ^f	171800+5930	$S_{24} \geq 4.6$	0.001157	46	L07 wedge	mix, see L07	100	4.6	45
XFLSDeep ^f	171517+5956	$0.61 \leq S_{24} < 4.6$	0.0002735	178	Exp. wedge	MMT/Hectospec	91	0.61	175

Notes:-

^a number of objects with either spectroscopy attempted, or literature redshifts.

^b number of objects in the 90% complete samples.

^c redshift quality (see Section 4.1)

^d *Spitzer* photometry from SWIRE (Lonsdale et al. 2003)

^e *Spitzer* photometry from SCOSMOS (Sanders et al. 2007)

^f *Spitzer* photometry from the Extragalactic First Look Survey (Lacy et al. 2005; Fadda et al. 2006)

Table 2: Mid-IR-selected AGN candidates and follow-up spectroscopy log

Object Name	Sample	Telescope/ Instrument (or literature reference)	Observation Date (UT)	Exposure Time (s)	MagSys ^a	m_1	m_2	m_3	m_4	m_5	oflg ^b	oref ^c	Z	Y	J	H	K	nflg ^d	nref ^e
SW002644.79-430958.1	ELAIS-S1Bright	SOAR/Goodman	2008-08-01UT	900	Vega:UBVRI		19.47				29	APM							64
SW002802.45-424913.5	ELAIS-S1Bright	6dF			Vega:UBVRI				17.6		23	6dF							64
SW002802.79-425957.0	ELAIS-S1Bright	SOAR/Goodman	2008-08-03UT	3×900	Vega:UBVRI		20.28				29	APM							64
SW002927.72-431614.4	ELAIS-S1Bright	Gemini-S/GMOS	2008-10-10UT	3×900							64								64
SW002933.86-435240.4	ELAIS-S1Bright	LF04			Vega:UBVRI				17.7		23	LF04							64
SW002959.22-434835.1	ELAIS-S1Bright	LF04			Vega:UBVRI				17.42		23	LF04							64
SW003114.45-424227.7	ELAIS-S1Bright	LF04			Vega:UBVRI				20.1		23	LF04							64
SW003224.37-424211.0	GMOS-S	Gemini/GMOS-S	2008-10-02UT	2×600							64								64

Notes:- Table 2 is published in its entirety in the electronic edition of Astrophysical Journal Supplement, a portion is shown here for guidance regarding its form and content. Note that we also include sources that satisfied our selection criteria, but which lack spectroscopic observations for completeness. Literature references: 2dF - Colless et al. 2001; 6dF - Jones et al. 2009; FBQS - White et al. 2000; LF04 - La Franca et al. 2004; Mao12 - Mao et al. (2012); P06 - Papovich et al. (2006); RC3 - de Vaucouleurs, G. et al. 1991; S01 - Serjeant et al. 2001; S-A94 - di Serego-Alighieri et al. 1994; S06 - Simpson et al. 2006; S12 - Simpson et al. (2012); Sh02 - Sharp et al. 2002.

^a Optical magnitude system and filters: AB or Vega denotes the system, followed by a colon, then the filter set used in the next five columns ($m_1 - m_5$) (i.e. Vega:UBVRI or AB:ugriz). (Note that all the near-IR magnitudes, Z, Y, J, H, K , are in the Vega system.)

^b Bit flag indicating which optical magnitudes are limits or missing, values are added to the bit flag as follows: 1- m_1 is a limit/missing, 2- m_2 is a limit/missing, 4- m_3 is a limit/missing, 8- m_4 is a limit/missing, 16- m_5 is a limit/missing. For example, a bit flag of 17 (1+16) indicates that m_1 and m_5 are missing/limits, and the remainder of m_2, m_3 and m_4 are detections. Where limits are known, they are given, otherwise the magnitude column is left blank. An oflg of 64 indicates that no optical detection has been reported for this object.

^c Source of the optical data. APM - Maddox et al. (1990); CASU - González-Solares et al. (2011); CFHTLS - Gwyn (2012); COSMOS - Sanders et al. (2007); ESIS - Berta et al. (2006); LCRS - Schechtman et al. 1996; MS4 - Burgers & Hunstead (2006); SDSS - Abazajian et al. 2007; SWIRE - Lonsdale et al. (2003; <http://swire.ipac.caltech.edu>); USNO-A2 - <http://ftp.nofs.navy.mil/projects/pmm/catalogs.html>). Others as for the spectroscopic references above. "This paper" refers to estimates from spectroscopic acquisition images, or by-eye estimates from available imaging, with an uncertainty ≈ 0.5 magnitudes. The other magnitudes are accurate to ≈ 0.1 magnitudes or better, see the respective papers for details. CASU and SWIRE magnitudes are aperture magnitudes in 2.4 or 3.1 arcsecond diameters, respectively. The remainder are estimated total magnitudes ("MAG_AUTO" in SExtractor, Bertin & Arnouts [1996]).

^d Bit flag indicating which near-infrared flags are limits or missing, values are added to the bit flag as follows: 1- Z is a limit/missing, 2- Y is a limit/missing, 4- J is a limit/missing, 8- H is a limit/missing, 16- K is a limit/missing. The resulting nflg is then calculated by summing these values. Where limits are known, they are given, otherwise the magnitude column is left blank. An nflg of 64 indicates that no near-infrared detection has been reported for this object.

^e Source of the near-infrared data. 2MASS - Strutskie et al. (2006); DXS, UDS - the Deep Extragalactic Survey and Ultra-Deep Survey of the United Kingdom Infrared Deep Sky Survey (UKIDSS) (Lawrence et al. 2007). VIDEO - Jarvis et al. (2013). For DXS and UDS the 2 arcsecond diameter apertures are quoted, for VIDEO the Petrosian magnitudes. "This paper" refers to estimates from spectroscopic acquisition images, with an uncertainty ≈ 0.5 magnitudes. The other magnitudes are accurate to ≈ 0.1 magnitudes or better, see the respective papers for details. Note that all near-infrared magnitudes are on the Vega system.

6

Table 3: Properties of the AGN in the spectroscopic survey.

Object Name	Sample	In statistical sample?	Redshift	Redshift quality ^a	Type ^b	Type quality ^c	$S_{3.6}$ (μJy)	$S_{4.5}$ (μJy)	$S_{5.8}$ (μJy)	$S_{8.0}$ (μJy)	S_{24} (μJy)
SW002644.79-430958.1	ELAIS-S1Bright	Y	0.241	1	3	2	393.79	480.71	605.92	1890.67	9629.14
SW002802.45-424913.5	ELAIS-S1Bright	Y	0.127	1	1	1	1260.01	1529.63	2171.13	3210.09	13819.66
SW002802.79-425957.0	ELAIS-S1Bright	Y	1.731	2	4	2	464.41	842.38	1655.11	3256.47	11582.89
SW002927.72-431614.4	ELAIS-S1Bright	Y	0.593	1	2	1	307.22	409.86	647.29	940.93	5804.15
SW002933.86-435240.4	ELAIS-S1Bright	Y	0.994	1	1	1	842.44	1183.64	1701.33	2374.71	7102.62
SW002959.22-434835.1	ELAIS-S1Bright	Y	2.039	1	1	1	571.40	832.07	1501.68	2611.84	6321.39
SW003114.45-424227.7	ELAIS-S1Bright	Y	0.593	1	1	1	1108.38	1744.93	2532.70	4025.79	11810.21
SW003119.19-424533.9	GMOS-S	Y	0.494	1	3	1	184.00	150.00	139.00	235.00	1013.00

Notes:- Redshift quality, type and type quality flags are discussed in detail in Sections 4.1 and 4.2, and are summarized here:

^a redshift quality: 1-secure redshift based on two or more high signal-to-noise features; 2-less secure redshift, based on multiple features, but with only one or fewer detected at high signal-to-noise; 3- uncertain redshift, based on weak spectral features, or a single strong line; 4- featureless spectrum, no redshift estimate.

^b type: 1- normal, unobscured type-1 AGN; 2- heavily obscured, type-2 AGN; 3- no indication of an AGN in the optical spectra; 4- lightly obscured AGN, with broad-lines visible in the rest-frame optical, but a red continuum.

^c type quality: 1- secure classification (broad lines for type-1s, BPT diagram, [NeV] emission or high-ionization UV lines and a rest-frame optical spectrum for type-2s; clear $(g-i)^*$ color excess compared to normal quasars); 2- less secure classification (e.g. only partial information for BPT, low signal-to-noise high-ionization line detections); 3 or 4- uncertain classification due to lack of strong spectral features and/or uncertain line identification.

Table 3 is published in its entirety in the electronic edition of Astrophysical Journal Supplement, a portion is shown here for guidance regarding its form and content.

we were able to obtain near-infrared spectra with IRTF using Spex (Rayner et al. 2003), Gemini with NIRI (program GN2009B-C-8) and Triplespec (Herter et al. 2008) on Palomar. The near-infrared observations are listed in Table 4, and the corresponding spectra are shown in Figures 3-6.

4. Redshifts and Spectral classifications

4.1. Redshift completeness and quality flags

Redshifts and classifications for the objects are shown in Table 3 (full table in the electronic edition). Objects were assigned a redshift quality flag from 1-4 according to the following criteria:

1. Secure redshift based on the high signal-to-noise ($> 10\sigma$) detection of two or more spectral features (in emission or absorption).
2. Less secure redshift, based on the detection of one emission line at high signal-to-noise plus one line at lower signal-to-noise ($> 3\sigma$), or more than two lines at lower signal-to-noise.
3. Uncertain redshift based on a single weak line with only weak secondary features to obtain the redshift, or a single strong line whose identity was deduced from its profile or the absence of other lines expected to be similarly strong in the spectrum.
4. Featureless spectrum, or spectrum with only a single weak line and no other features (no redshift assignment attempted).

Objects with redshift quality 2 or 3 were also checked for plausibility with the assumed

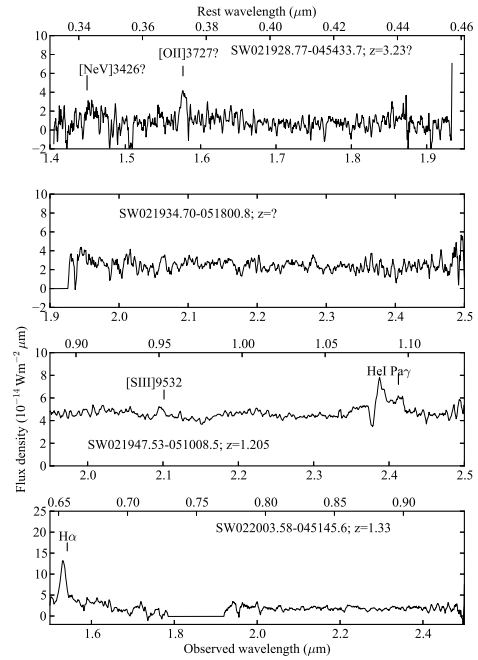


Fig. 3.— Near-infrared spectra of high redshift objects in the XMMDeep sample.

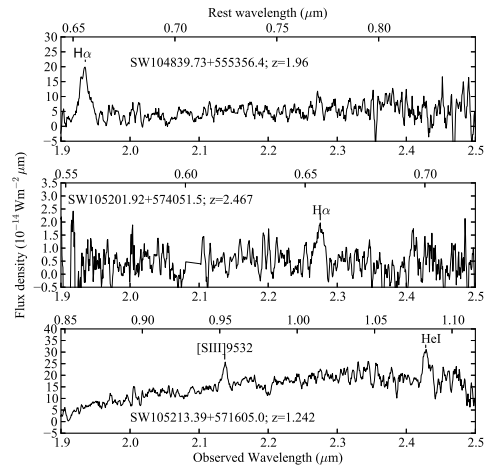


Fig. 4.— Near-infrared spectra of high redshift objects in the LockmanBright and LockmanDeep samples.

Table 4: Near-infrared spectroscopy

Object	Subsample	Telescope	Instrument/Band	Integration time	Observation date
SW 021928.77-045433.7	XMM-LSSDeep	Gemini-N	NIRI/H	37x120	2009-11-29
SW 021934.70-051800.8	XMM-LSSDeep	Gemini-N	NIRI/K	37x120	2009-11-28
SW 021947.53-051008.5	XMM-LSSDeep	Gemini-N	NIRI/K	13x120,18x120	2009-12-08,09
SW 022003.58-045145.6	XMM-LSSDeep	Gemini-N	NIRI/J,K	31x120,37x120	2009-11-29,2009-11-30
SW 022003.58-045145.6	XMM-LSSDeep	Hale	Triplespec	8x300	2008-07-27
SW 104839.73+555356.4	LockmanBright	Gemini-N	NIRI/K	26x120	2009-11-29
SW 105201.92+574051.5	LockmanDeep	Gemini-N	NIRI/K	25x120	2009-11-28
SW 105213.39+571605.0	LockmanDeep	Gemini-N	NIRI/K	19x120	2009-11-28
SW 160913.28+542322.0	LockmanDeep	Hale	Triplespec	20x300	2011-07-12
SW 163313.28+401338.9	EN2Bright	Hale	Triplespec	12x300	2011-07-11
XFLS 171053.51+594433.1	XFLSFaint	Hale	Triplespec	24x300	2011-07-11
XFLS 171419.9+602724	XFLSBright	IRTF	Spex	30x120	2007-06-18
XFLS 171503.96+595959.3	XFLSFaint	Hale	Triplespec	24x300	2011-07-12
XFLS 171702.54+600620.7	XFLSFaint	Hale	Triplespec	16x300	2011-07-11
XFLS 171754.6+600913	XFLSBright	IRTF	Spex	30x120	2007-06-19

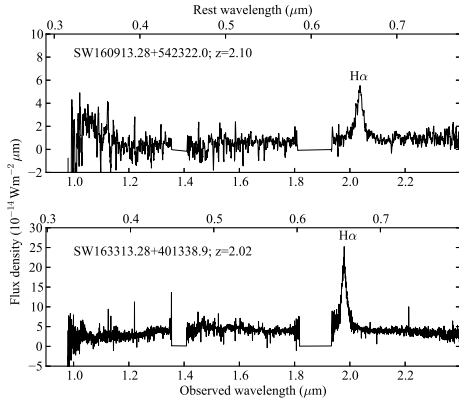


Fig. 5.— Near-infrared spectra of high redshift objects in the ELAIS-N1Bright and ELAIS-N2Bright samples.

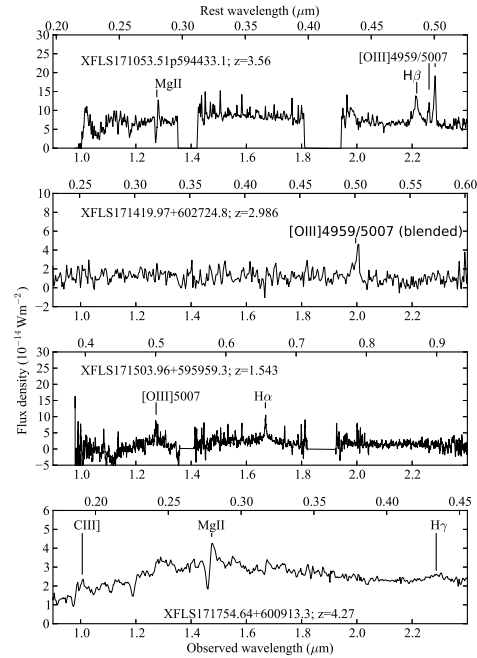


Fig. 6.— Near-infrared spectra of high redshift objects in the XFLSBright and XFLSFaint samples.

redshift using SED fitting using models similar to those in Lacy et al. (2007b). In cases that these led to unphysical SEDs (for example, host galaxy masses $\gg 10^{12} M_{\odot}$, or significant dust emission corresponding to dust temperatures above the sublimation temperature of $\approx 1500\text{K}$), the redshifts were assumed to be incorrect and redshift quality set to 4. Full details of the SED fitting will be given in Lacy et al. (2013). Figure 7 shows the distribution of redshift quality by object classification (see Section 4.2 below). As expected, the unreddened AGN have the lowest fraction of poor quality redshifts. The redshift distribution of the non-AGN cuts off abruptly at $z \approx 1$, probably because higher redshift objects in this class lack strong emission features in their rest-frame UV spectra, so would have featureless spectra.

Overall redshift completeness in the samples varied from 100% for most of the bright samples, to $\sim 20\%$ for some of the faint samples. In order to obtain a subset of the survey useful for statistical purposes in Ridgway et al. (2013), a $\geq 90\%$ complete subsample was computed for each individual sample by exploiting the correlation of S_{24} with emission line flux (except for GMOS-S, which has a very narrow range in S_{24}). This was carried out as follows: each sample was sorted in descending order of S_{24} . The completeness was then calculated as a function of S_{24} (assuming all redshifts with qualities 1-3 were correct). Objects were included in the 90% complete sub-sample until the completeness as a function of S_{24} dropped below 90% for the final time (see Table 1). These 90% complete samples, combined with the 81% complete GMOS-S sample constitute the “statistical sample” of 662 objects.

The histogram of redshifts broken up by type (as described below), together with the $24\mu\text{m}$ flux distribution of the objects lacking redshifts are shown in Figure 8. As ex-

pected, most of the objects lacking redshifts are faint at $24\mu\text{m}$ (see Section 8). There does seem to be a deficit of type-2 objects with $1.4 < z < 1.6$ analogous to the traditional “redshift desert” for normal galaxies, when [OII]3727 redshifts out of the optical band and before Ly α redshifts in (see also the top-right panel of Figure 7). For our type-2 objects, the CIV 1549 line is typically brighter than Ly α , which is we believe why the redshift desert for our objects extends only to $z \approx 1.6$, where CIV is shifted to 4000\AA , the blue end of most of our spectra. The type-1 objects are not affected by this, as they have strong low-ionization broad lines (MgII 2798 and CIII]1909) in the observed optical bands at these redshifts. These low-ionization UV lines tend to be relatively weak in the type-2s (see Section 9). The dip may also be in part due to the fact that samples flux limited at $24\mu\text{m}$ containing heavily obscured objects are biased against these redshifts as the $9.7\mu\text{m}$ silicate feature is redshifted into the $24\mu\text{m}$ band in this range.

4.2. Classification

Objects were classified as either type-1 (normal, unobscured; type=1 in Table 3), type-2 (heavily obscured; type=2 in Table 3), lightly obscured, with broad lines visible in the rest-frame optical, but a red continuum (type=4 in Table 3), or showing no evidence for an AGN in their optical spectra (type=3 in Table 3.1, called “non-AGN” in the text of this paper, although some of them in fact are AGN based on other criteria, see Section 7). There are also 24 stars, most likely contaminants due to saturated IRAC flux densities (though probably possessing debris disks to be bright at $24\mu\text{m}$), classified as type=5. The criteria followed those employed by L07, based principally on emission line properties (presence of broad lines, classification on BPT diagrams, presence of [NeV] emission or pres-

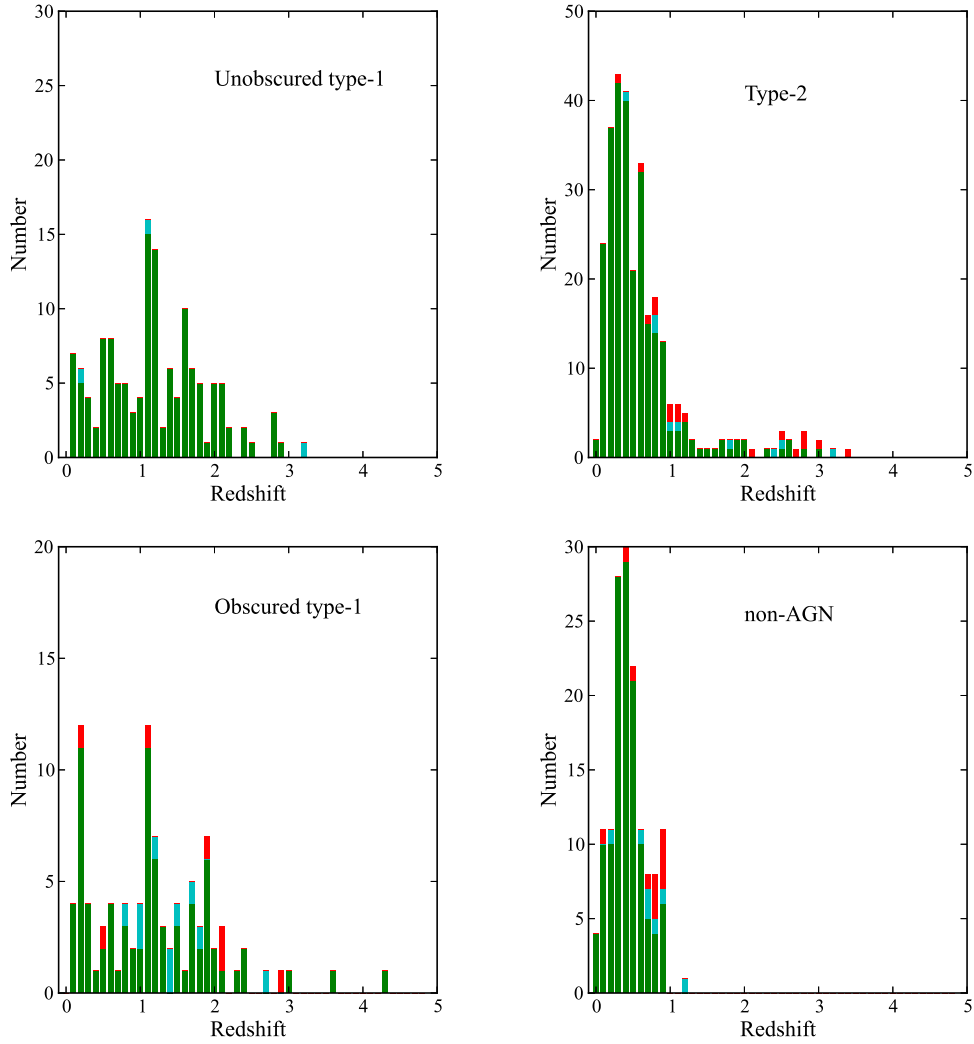


Fig. 7.— Histograms of redshift for each of the four classes of object. Objects with redshift quality 1 are shown in green, those with redshift quality 2 in blue, and those with redshift quality 3 in red.

ence of high ionization UV lines in emission), although a more refined definition of dust-reddened versus normal AGN was used, as described below. Where possible, a rest-frame optical spectrum was used to distinguish between a type-2 AGN and a lightly obscured AGN. Objects with uncertain types have type quality two or greater. Typically these are objects which lack a full set of detected lines to plot on a diagnostic diagram, or are high redshift without a rest-frame optical spectrum.

We can be fairly sure that objects showing narrow, high ionization UV emission lines are AGN based on comparison with radio galaxies and X-ray detected type-2 quasars (e.g. Norman et al. 2002). Although high ionization resonant emission lines such as SiIV 1402Å and CIV1548/1551Å can be formed in starbursts, in the stellar winds and photospheres of the most massive stars, as well as the interstellar medium (e.g. Robert, Leitherer and Heckman 1993), they are predicted to form P-Cygni profiles, with substantial absorption from gas blueshifted along the line of sight, which we do not see in our objects. Furthermore, in practice, Lyman break galaxies show high-ionization species predominantly in absorption (Shapley et al. 2003). High ionization species which do appear in emission, such as HeII 1640Å and CIII] 1909Å tend to have very low rest-frame equivalent widths (RFEWs) ($\lesssim 2\text{Å}$). We also have several known examples of objects which show narrow lines in the rest-frame UV, but broad lines in their near-infrared, rest-frame optical spectra (e.g. XFLS 171053.51+594433.1), which reinforce the point that near-infrared spectra are needed for accurate classification as a type-2 versus a reddened type-1 object. For objects which lack near-infrared spectroscopy, we have been able to make an approximate classification based on SED shapes, however, these are uncertain and have type quality =2 or 3.

A significant fraction of our mid-infrared selected AGN have broad-line spectra, but are clearly redder than the optically-selected quasar population (the objects classified as type=4 in Table 3). This red AGN population has also been found in other surveys based on selection from the Two Micron All Sky Survey (2MASS) (e.g. Cutri et al. 2003) or 2MASS and the Faint Images of the Radio Sky at Twenty-centimeters (FIRST) radio survey (e.g. Glikman et al. 2005; 2008; Urrutia et al. 2009). Classification of red versus normal AGN needs to take into account (at least in a statistical sense) the intrinsic variation in AGN colors, and be empirically based, so as not to be tied to a specific reddening law. We have adopted the technique of Richards et al. (2003), who use the $g - i$ color excess relative to the mean for SDSS quasars as a measure of reddening. They argue that intrinsic color variations are likely to be symmetrically distributed around the mean color, and that the objects with red excesses beyond this distribution are likely to be reddened by dust. Most of our objects have photometry on the SDSS system, and thus we are able to use the $(g - i)$ reference colors as a function of redshift from Richards et al. to calculate the distribution of excess $(g - i)$ color, $(g - i)^*$, for the 193 of our objects which are classified as type-1 (normal or reddened) and have photometry on the SDSS system (samples XMM-LSSBright, XMM-LSSDeep, LockmanBright, LockmanDeep, EN1Bright, EN1Deep, EN2Bright, XFLSBright, XFLSDeep), shown in Figure 9(a). The peak around zero reddening has a standard deviation (after clipping) of ≈ 0.15 magnitudes. We therefore place our empirical boundary between reddened and unreddened objects two standard deviations away, at $(g - i)^* = 0.3$. This adoption of an observed-frame color to distinguish red from normal AGN does mean that the reddening in the rest-frame at which this occurs

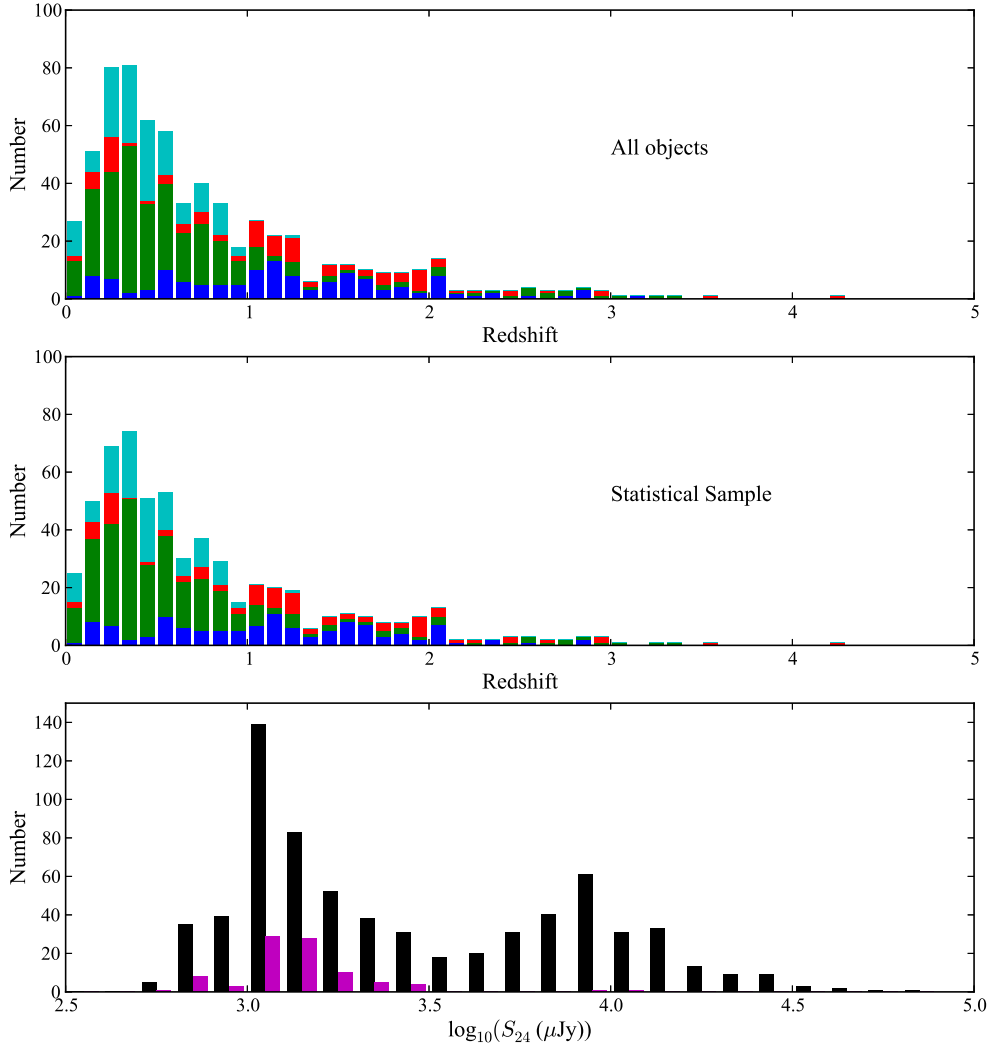


Fig. 8.— Histograms of redshifts by object type: type-1 objects are shown in blue, type-2 objects in green, reddened type-1 objects in red and objects with non-AGN optical spectra in cyan. The bottom histogram shows the $24\mu\text{m}$ flux distribution for the objects with featureless spectra (magenta) compared to the remainder of the sample (black).

will vary as a function of redshift (as a given optical depth of dust will result in a higher $(g - i)^*$ in high redshift objects), however, only a handful of objects have colors close enough to the boundary to make their classifications uncertain due to this. The rest-frame $E(B - V)$ obtained from fitting a reddened template quasar SED to SEDs of objects close to our proposed boundary implies that a $(g - i)^*$ color excess of 0.3 magnitudes corresponds to an $E(B - V) \approx 0.1 - 0.15$ at $z \sim 1$, previously used by us to define red quasars (e.g. Urrutia et al. 2009). The 24 objects without colors on the SDSS system (objects in the GMOS-S, CDFSBright, ES1Bright and ES1Deep samples) were evaluated on the basis of available optical colors as close to g and i as possible. In most cases classification was unambiguous, however, in five cases which were close to the estimated boundary a classification of unreddened was used.

We also used the SED of Richards et al. (2006) to calculate the $r - [24]$ color excess between the optical and mid-infrared, $(r - [24])^*$ (Figure 9(b)). There is a clump of normal AGN near $(0, 0)$, consistent with the idea that we are dominated by the normal AGN population, and are not systematically selecting objects with unusually bright infrared emission. As expected for dust reddening, $(g - i)^*$ correlates broadly with $(r - [24])^*$, though the correlation is surprisingly poor. The objects scattered towards bluer $(r - [24])^*$ colors seem to be explained in terms of host galaxy contamination, as the majority of objects in this area of the plot are of low redshift and show evidence of host galaxy starlight in their spectra. Conversely, the outliers with high $(r - [24])^*$ and low $(g - i)^*$ tend to be objects very faint in the optical, where again host galaxy emission and (possibly) scattered AGN light may make the observed colors bluer. The lack of a tight correlation for the more highly reddened

objects (redder than $(g - i)^* = 0.3$) may also reflect genuine variation in the ratio of reddening (measured by $(g - i)^*$) to optical extinction (approximated by $(r - [24])^*$) in our population.

5. X-ray detections

We matched the objects in our spectroscopic survey in Table 3 to the 2XMM-DR3 catalog of serendipitous XMM sources (Watson et al. 2009) and the *Chandra* Source Catalog (CSC; Evans et al. 2010), finding 108 matches to 2XMM and 81 to the CSC (36 of which are in both catalogs) (Table 5). Both catalogs have only patchy coverage across the survey fields, and exposure times ranging from $\sim 5 - 50$ ks, so the low detection fraction is no surprise. As pointed out in L07 and Donley et al. (2012), though, many obscured AGN are not detected even in deep X-ray surveys. The breakdown, among the X-ray detected sources, by type is 52 normal type-1s, 45 type-2s, 31 red type-1s, nine objects with redshifts but no optical AGN signatures, 14 objects with featureless spectra and two stars. Four of the 2XMM sources and one of the CSC sources are weaker than $10^{42} \text{ergs}^{-1} \text{cm}^{-2}$, where their X-ray luminosity could plausibly be powered by X-ray binaries in the host galaxy (e.g. Teng et al. 2005), but the vast majority are much more luminous, and almost certainly powered by AGN.

Figure 10 plots the X-ray flux against the $24\mu\text{m}$ flux, the histogram of the X-ray to $24\mu\text{m}$ flux ratio and the distribution of hardness ratio (HR) by type (for XMM we use *HR2*, defined to be that between 0.5-1keV and 1-2keV, for *Chandra* we use the HR defined between the “hard” and “soft” ACIS bands, called *HRC* in this paper), and the X-ray luminosity versus the mid-infrared luminosity. The mid-infrared k-correction is calculated using the measured 8- $24\mu\text{m}$ spectral index. For both the 2XMM and CSC

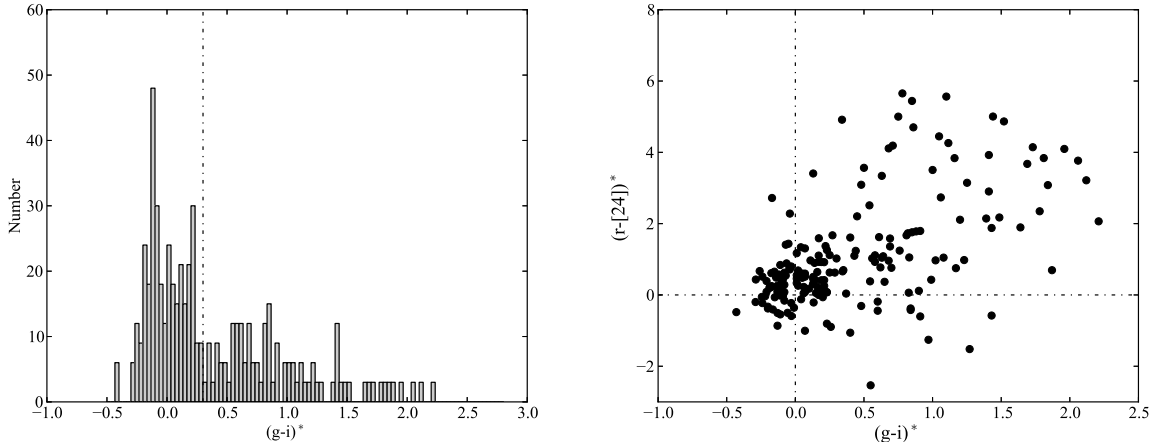


Fig. 9.— *Left* (a) histogram of corrected $g - i$ color for the objects classified as type-1 (i.e. having broad lines in the rest-frame optical). *Right* (b) excess $g - i$ color plotted against corrected $r - [24]$ color for the broad-line objects.

detections, the type-1 objects are generally the brightest and softest in X-rays (mean HRC , $\langle HRC \rangle = -0.13$ with a dispersion of ± 0.25 , mean $HR2$, $\langle HR2 \rangle = 0.02 \pm 0.25$) and their X-ray fluxes correlate loosely with the $24\mu\text{m}$ flux. The type-2s and other obscured populations are, on average, the faintest and have a wide range of hardness ratios ($\langle HRC \rangle = 0.14 \pm 0.37$; $\langle HR2 \rangle = 0.15 \pm 0.48$ for Type-2s, $\langle HRC \rangle = -0.04 \pm 0.31$; $\langle HR2 \rangle = 0.31 \pm 0.35$ for red type-1s, $\langle HRC \rangle = -0.14 \pm 0.22$; $\langle HR2 \rangle = 0.45 \pm 0.53$ for optically-classified “non-AGN”, and $\langle HRC \rangle = 0.21 \pm 0.34$; $\langle HR2 \rangle = 0.40 \pm 0.37$ for objects with featureless optical spectra. If we were to reclassify objects purely on the basis of their X-ray hardness ratios, and assumed a division of $HRC = 0$ or $HR2 = 0.1$ as the boundary of “obscured” versus “unobscured”, 19% (12/62) of the optically-classified unobscured type-1 objects would be classed as obscured in the X-ray. Conversely, 41% (24/59) of the type-2 objects would have been classified as X-ray unobscured, along with 51% (19/37) of the reddened type-1 objects, 50% (5/10) of the objects with non-AGN spectra, and 26% (7/12) of the objects with featureless spec-

tra. These differences are, however, subject to systematic uncertainties as we only consider X-ray detected objects, and the obscured objects in particular tend to be faint, rendering their hardness ratios uncertain, and subject to contamination by soft emission from scattering of AGN emission, or X-ray binaries in the hosts. Nevertheless our results are consistent with those of Brightman & Nandra (2011), who also note discrepancies between X-ray and optical classifications of AGN. On the X-ray luminosity – mid-infrared luminosity plots the correlation for the 2XMM points (whose fluxes are more weighted towards the soft X-rays) is less tight than for the 2-10keV *Chandra* luminosities.

6. Radio detections

The fields used for this survey overlap with several moderate depth (root mean square (RMS) sensitivity $\approx 10\text{-}30\mu\text{Jy}$) radio surveys at 1.4GHz. In the north, the XFLSBright and XFLSDeep samples overlap with the Very Large Array (VLA) survey of Condon et al. (2003), the LockmanDeep sample overlaps with the Ibar et al. (2009) VLA survey and the ELAIS-N1Deep sample overlaps with the

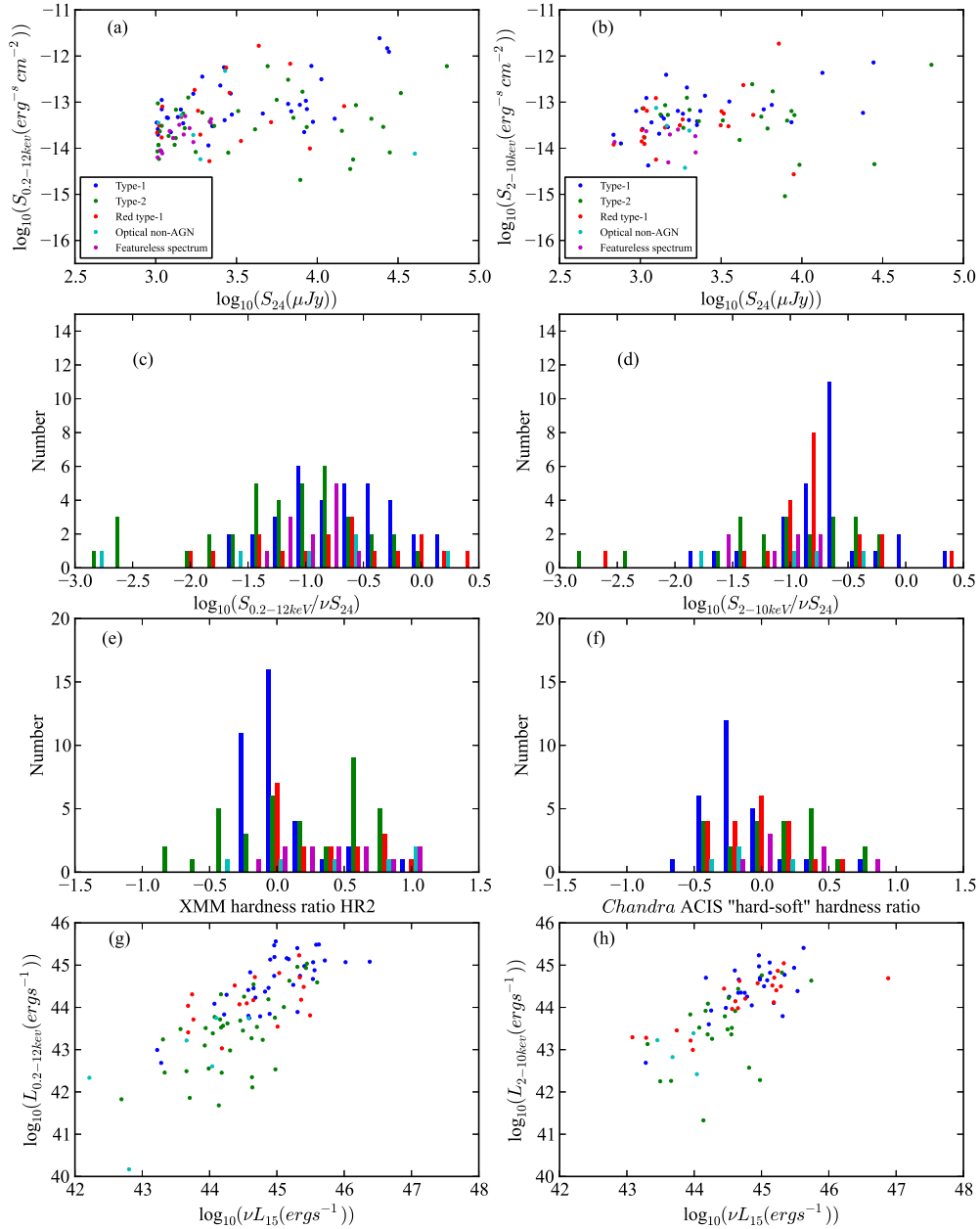


Fig. 10.— X-ray detections and hardness ratios of objects in the survey by type. (a) XMM 0.2–12keV flux versus $24\mu\text{m}$ flux density, (b) *Chandra* 2–10keV flux versus $24\mu\text{m}$ flux density, (c) ratio of XMM 0.2–12keV to $24\mu\text{m}$ flux, (d) ratio of *Chandra* 2–10keV flux to $24\mu\text{m}$ flux, (e) distribution of XMM hardness ratio HR2, (f) distribution of *Chandra* hardness ratio, (g) XMM luminosity versus $15\mu\text{m}$ luminosity, and (h) *Chandra* luminosity versus $15\mu\text{m}$ luminosity. The color coding of the histograms is given in the top panels.

Table 5: X-ray properties of AGN in the spectroscopic survey

Name	Redshift	Type	S_{24} (μJy)	CSC Name	CSC 2-10keV flux ($\text{ergs}^{-1}\text{cm}^{-2}$)	CSC HR (h-s)	2XMM Name	2XMM 0.2-12keV flux ($\text{ergs}^{-1}\text{cm}^{-2}$)	2XMM HR2
SW0003312.39-431841.9	0.248	1	1030.0	CXO J0003312.3-431842	2.61E-14	0.716161	2XMM J0003312.3-431841	2.60E-14	0.93102986
SW0003316.92-431706.3			2200.0	CXO J0003316.9-431706	8.12E-15	0.375333	2XMM J0003317.0-431705	4.29E-14	0.917
SW0003330.42-431554.3	0.437	3	1890.0	CXO J0003330.4-431554	3.77E-15	-0.325	2XMM J0003330.4-431552	5.79E-15	1.0
SW0003333.75-432326.9			1490.0	CXO J0003333.7-432326	4.94E-15	0.0643	2XMM J0003333.7-432328	1.98E-14	0.651
SW0003336.26-431731.7			2190.0	CXO J0003336.2-431731	1.82E-14	0.482	2XMM J0003336.1-431732	3.58E-14	0.837
SW0003346.28-431943.7	0.402	2	3240.0	CXO J0003346.2-431943	4.02E-14	0.025	2XMM J0003346.2-431944	6.40E-14	0.176
SW0003357.32-433601.7	1.932	4	1060.0	CXO J0003357.2-433602	1.24E-14	-0.341			

Notes:- This table contains the matches in the CSC and 2XMM catalogs to all the objects in Table 3 (which have with either spectroscopy from the literature or from our own observations). Objects with featureless spectra are included (with the redshift and type columns left blank). Table 5 is published in its entirety in the electronic edition of Astrophysical Journal Supplement, a portion is shown here for guidance regarding its form and content.

VLA survey of Ciliegi et al. (1999). In the south, the ELAIS-S1Bright, ELAIS-S1Deep and CDFSBright surveys overlap the Deep Australia Telescope Large Area Survey made with the Australia Telescope Compact Array (ACTA) (Norris et al. 2006; Middelberg et al. 2008). We have cross-matched our survey AGN with the public source lists from these surveys in order to make an initial examination of the radio properties of our objects, detecting 214 objects. In the XFLS-Bright and XFLSDeep fields, which overlap the deep (RMS $10\mu\text{Jy}$) and uniform radio survey of Condon et al., our detection rate is 90/223, or 40%, so even in the fields with the best radio data the majority of objects remain upper limits.

Figure 11 shows the flux-flux plot, the luminosity-luminosity plot and a histogram of radio loudness (where we define the k-corrected infrared radio-loudness as:

$$R_{IR}^* = \log_{10}(F_{5GHz}/F_{15\mu m})$$

where F_{5GHz} and $F_{15\mu m}$ are the rest-frame fluxes at 5GHz and $15\mu m$, respectively). A radio spectral index $\alpha = -0.8$ (where flux density $S_\nu \propto \nu^\alpha$) was assumed. We also show the approximate position of the far-infrared – radio correlation adapted from Appleton et al. (2004) with a small (-0.2 dex) correction to allow for the different infrared and radio wavelengths used.

Most AGN lie close to the far-infrared – radio correlation, even when the mid-infrared, which is dominated by AGN luminosity, is used, as has been noted in the past (Sopp & Alexander 1991; Kimball et al. 2011). We also see no sign of any radio-loudness dichotomy or bimodality in any of our object classifications, consistent with most recent studies (White et al. 2007; Kimball et al. 2011). We do, however, see significant scatter both above the far-infrared – radio relation (the expected radio-loud/intermediate population) and be-

low (where objects with strong AGN-related mid-infrared emission appear). Furthermore, the distribution of R_{IR}^* values for the broad-line objects (with a mean of -1.35 with an error in the mean of ≈ 0.1 for both the normal and obscured type-1 populations) is lower than that for the type-2 population (-1.09 ± 0.05) and the non-AGN (-1.05 ± 0.05). We performed both a Mann-Whitney U -test and a t -test to investigate whether the values of R_{IR}^* are systematically lower for the broad-line objects taken as a group versus the type-2s, finding a 3% probability of the samples being drawn from identical parent populations in both cases. Thus the difference is not highly robust, and, furthermore, the large number of upper limits may mean that the result may be biased by the different redshift and luminosity distribution of the broad line and type-2 populations (although there is no obvious luminosity dependence in Figure 11). If this result is real, however, one interpretation can be obtained if we assume that the intrinsic mean ratio of mid-infrared to radio emission is the same for both populations, but that the type-2s have some extinction towards the mid-infrared, even at $15\mu\text{m}$. This is broadly consistent with the work on radio-loud AGN by Cleary et al. (2007) and Haas et al. (2008), where the infrared SEDs of radio galaxies and radio-loud quasars matched in radio luminosity differ by a factor ≈ 3 at $12\mu\text{m}$ (i.e. very similar to our \approx factor of two difference at $15\mu\text{m}$), despite having similar total FIR luminosities, and may also be supported by our tentative findings in Section 8 regarding the optical depth of the torus. However, this must remain speculative pending better radio data and consideration of the full infrared SEDs and demographics of these objects.

7. The nature of objects lacking AGN signatures in the optical

A significant fraction (22%) of our objects with redshifts show no clear AGN signatures in their optical spectra and are classified as “non-AGN”. Where spectral features are seen, these objects have low ionization emission line spectra. An additional 15% of our candidates have featureless spectra or spectra with only a single, unidentifiable faint line (redshift quality=4). They are excluded from our AGN sample, but may contain AGN with both the NLR and AGN continuum/broad-line region heavily obscured. In Figure 2 they are spread throughout the selection region, some close to the edges, suggesting that indeed they are interlopers, but some are directly along the AGN locus, and satisfy the Donley et al. (2012) selection criteria. In a few of the objects we have ancillary information indicating an AGN. Nine objects with “non-AGN” spectra are detected in the 2XMM or CSC catalogs, including SW021822.13-050614.1, which Severgnini et al. (2003) show has faint AGN emission lines in its nuclear spectrum once a host galaxy template is subtracted from a deep optical spectrum. 14 objects with optically-featureless or single emission line spectra are detected in X-rays. Finally, one object is radio-intermediate, with $R_{IR}^* = 0.13$ (SW160857.99+541818.4) and one object, XFLS171115.2+594906, has a flat radio spectrum, indicative of its radio emission arising from an AGN (a spectral index between 610MHz and 1.4GHz of $\alpha = -0.3$, where radio flux density $S_\nu \propto \nu^\alpha$).

Based on comparing the X-ray detection rate of type-2 AGN and that of objects lacking AGN signatures we can place a rough lower bound on the number of AGN missing in our optically-classified sample. 45 optically-classified type-2 AGN are detected in X-rays, out of a total of 295 in the survey, a detec-

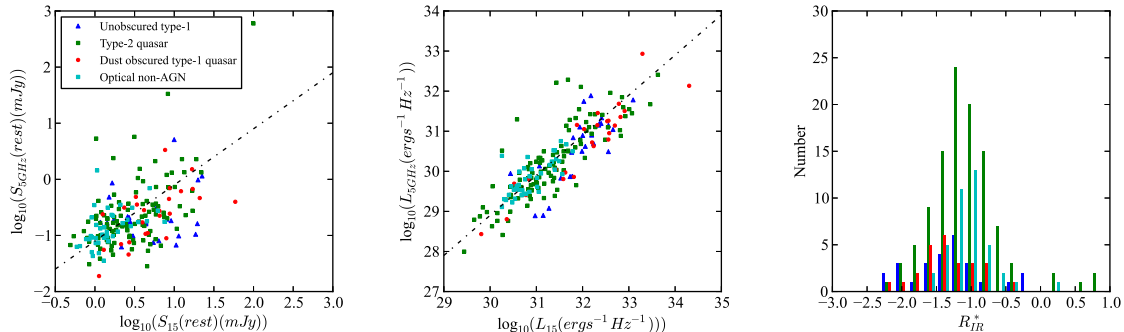


Fig. 11.— *Left* rest-frame 5GHz flux density plotted against rest-frame 15 μ m flux density, *middle* 5GHz luminosity as a function of 15 μ m luminosity, and *right* a histogram of radio-loudness, split by object type. The dot-dashed lines on the left and middle plots show the position of the far-infrared – radio correlation from Appleton et al. (2004), scaled to 15 μ m and 5GHz, assuming a mid-infrared spectrum flat in νf_ν and a radio spectral index of -0.8 .

tion rate of 15%. This compares to 23 objects with featureless spectra or otherwise no sign of AGN in their optical spectra, out of a total of 233 such objects in the survey, a detection rate of 10%, only a little lower than that of the type-2s. If we assume that the ratio of X-ray detected to X-ray undetected AGN is similar in the objects optically classified as “non-AGN” as it is in the type-2s this implies that at least $\approx 65\%$ of the objects classified as “non-AGN” on the basis of their optical spectra may in fact contain one.

8. The emission-line - mid-infrared luminosity correlation

Both the higher ionization emission lines and the mid-infrared emission are powered by UV emission from the AGN, so we expect these two quantities to correlate well. To test this, we measured the [OIII]5007 flux in normal type-1 and type-2 AGN spectra at $z < 0.75$, where this line is present in the optical spectra. As shown in Figure 12, the correlation exists between both fluxes and luminosities, with about a half dex scatter. The

origin of this scatter is unclear. Although we see evidence of dust reddening in the type-2 composite (see Section 9), the fact that the type-1 AGN plot among the type-2s and with similar scatter suggests that reddening is not the primary cause of the scatter. Other possibilities include variation in ionization level of the narrow-line region (NLR) (unlikely given the similarity of the NLR spectra we see), or variation in the covering factor of dust in the nuclear region. This latter explanation seems the most likely, though it is surprising that there is no strong correlation of this ratio with luminosity. Such a correlation would naturally occur in the simplest version of the “receding torus” model (Lawrence 1991; Simpson 2006), where (in the case of a torus optically thin in the mid-infrared) the mid-infrared luminosity should scale proportional to the covering factor of hot dust, ω , and the [OIII] luminosity should scale proportional to $(1 - \omega)$. The large scatter means that our result is probably consistent with the relatively weak dependence of covering factor with AGN luminosity found by Roseboom et al. (2012), though may be inconsistent with

the optically-thin torus case of Lusso et al. (2013) (and indeed Drouart et al. (2012) show that an optically-thick torus is a good fit to radio galaxy SEDs when using the radio core-to-lobe flux ratio to constrain the inclination of the torus).

9. Composite spectra

We constructed a composite spectrum for type-2 quasars, and also for the “non-AGN” class to search for evidence of weak AGN activity. Attempts to construct composites for the normal and reddened quasars did not result in useful spectra due to strong continua, which (particularly for the reddened quasars) varied considerably from object to object. The type-2 quasar composite was constructed using spectra from the bright samples (limiting fluxes $S_{24} > 4\text{mJy}$) only at $z < 0.8$ in order to exclude objects with Seyfert-like luminosities. At $z > 0.8$, all samples contained objects of quasar-like luminosity, so all available spectra were combined. We used only spectra from our observations in Table 2 that were of good quality (S/N on brightest line $\gtrsim 30$), and which had good sky subtraction. Two of the fiber spectra, SW160929.35+542940.8 and SW160828.55+542546 had a low-order continuum subtraction performed before addition as they had bad baselines due to poor sky subtraction.

The composite spectrum at wavelength λ_i was constructed as:

$$F(\lambda_i) = \frac{1}{\sum_j (w_j)} \sum_j w_j a_j f_j(\lambda_i)$$

where the sums are over all the spectra contributing at wavelength λ_i . The emission line flux scales approximately with the $24\mu\text{m}$ flux density S_{24} (see Figure 12), so the scale factor $a_j \propto 1/S_{24}^j$. The typical signal-to-noise, however, scales proportional to S_{24} (resulting in weights $w_j \propto S_{24}^j$).

The type-2 quasar spectrum (Figure 13) looks very similar to Seyfert-2 spectra, with strong high-ionization narrow lines, but also including low-ionization species such as [OI], consistent with the broad range of ionization expected from an AGN (though lacking the coronal lines seen in the Rose et al. (2011) spectrum of SDSS J113111.05+162739.5). The composite host galaxy shows multiple Balmer absorption features, consistent with a dominant stellar population $\lesssim 10^8\text{yr}$ old, as has been seen in the hosts of IR-luminous type-1 quasar hosts (Canalizo & Stockton 2000).

The “non-AGN” spectrum (Figure 14) was constructed from an average of all the spectra for the objects lacking AGN features in their optical spectra, it is restricted to the optical as there are no examples at $z > 1$ (at least not ones with detectable emission lines). The emission lines in both the individual spectra and the composite are more characteristic of starbursts than LINERs, as noted by L07, the number of candidate LINERs in these mid-infrared selected samples is very small, and we have no definitive LINER candidates. We have carefully examined our composite spectrum for signs of high ionization lines that could indicate the presence of a weak or highly obscured AGN but fail to find any conclusive evidence of these. Perhaps the best evidence from the composite that these objects are similar to the type-2s is the very similar host galaxy spectra, including Balmer absorption lines of similar equivalent width at H9 and higher. These objects could thus be obscured AGN with significant reddening towards the NLR, or simply lacking one. Nevertheless, we choose to exclude them from this AGN census until more unequivocal evidence for their AGN is found.

Table 6 compares the emission line fluxes from our Type-2 and non-AGN composites with the radio galaxy template from Mc-

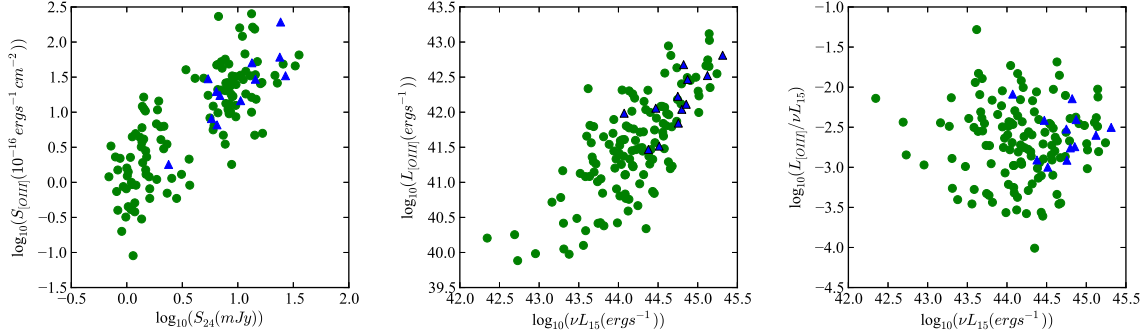


Fig. 12.— *Left* log of [OIII]5007 flux, $S_{[OIII]}$ plotted against S_{24} . *Middle* log of [OIII]5007 luminosity, $L_{[OIII]}$ plotted against $15\mu\text{m}$ luminosity (νL_{15}). *Right* log of the ratio of [OIII] to $15\mu\text{m}$ luminosity against $15\mu\text{m}$ luminosity. In all plots, type-2 AGN are plotted as green dots and type-1 AGN as blue triangles.

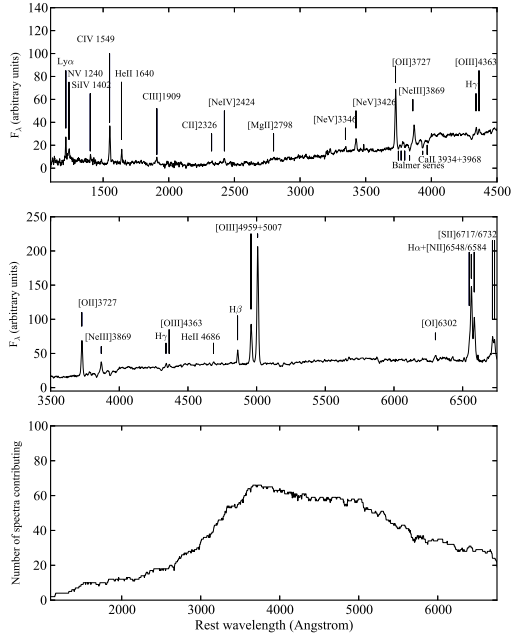


Fig. 13.— Type-2 quasar composite spectrum. The bottom panel shows the number of quasar spectra contributing at each wavelength.

Table 6: Line ratios in composite spectra relative to $H\beta$

Line	Wavelength (Angstrom)	Type-2 $f/H\beta$	Non-AGN $f/H\beta$	Radio Galaxy* $f/H\beta$	Case B $f/H\beta$
Ly α	1216	0.75	-	31	31
NV	1240	0.93	-	1.5	-
SiIV	1402	0.21	-	1.6	-
CIV	1549	1.45	-	3.6	-
HeII	1640	0.40	-	3.2	-
CIII]	1909	0.34	-	1.8	-
CII]	2326	0.16	-	0.92	-
NeIV]	2424	0.40	-	0.90	-
MgII	2798	0.75	-	0.78	-
NeV]	3346	0.16	-	0.20	-
NeV]	3426	0.53	<0.1	0.69	-
OII]	3727	2.78	2.5	3.64	-
NeIII]	3869	0.93	0.33	0.82	-
H γ	4340	0.19	-	0.24	0.47
OIII]	4363	0.18	<0.25	0.08	-
HeII	4686	0.18	-	0.20	-
H β	4861	1.0	1.0	1.0	1.0
OIII]	4959	3.9	0.38	3.1	-
OIII]	5007	10.8	0.99	8.7	-
OI]	6302	0.41	-	-	-
NII]	6548	1.4	-	-	-
H α	6563	7.0	-	-	2.9
NII]	6584	4.2	-	-	-
SII]	6717	2.3	-	-	-
SII]	6732	2.0	-	-	-

*McCarthy (1993)

Carthy (1993), and a Case B recombination model (for the hydrogen lines). Our type-2 composite spectrum shows evidence for reddening, in terms of significant Balmer decrements between $H\alpha$, $H\beta$ and $H\gamma$, and a weak $Ly\alpha$ line. There are also differences between the type-2 composite and that of the radio galaxies, in particular, the low-ionization UV lines (e.g. CIII] and CII] are weak compared to CIV in our composite when compared to radio galaxies) and the $Ly\alpha$ line is much weaker in the type-2 spectrum than in the radio galaxy composite. We speculate that this may be due to the effect of jet-induced shocks in the radio galaxies (a result consistent with the morphologies of extended emission line nebulae of type-2 quasars studied by Liu et al. 2013), but defer a detailed analysis to a future paper.

10. Discussion

Our survey of 786 objects with (attempted) spectra contains 672 extragalactic objects with redshifts (24 objects are stars included in error due to saturated flux densities in the IRAC bands, and 90 objects had featureless spectra). Of these, we have classified 136 as type-1 (normal quasars/Seyfert-1s), 96 as type-1 objects showing significant signs of reddening, 294 as type-2 quasars/Seyfert-2s, leaving 145 objects with redshifts, but showing no sign of AGN activity in their optical spectra. Our nested survey strategy has enabled us to span a wide range in luminosity ($>$ a factor of ten) at a given redshift. We classify 340 (50%) of the survey AGN as quasars based on their mid-infrared luminosities indicating that their bolometric accretion luminosities are $\gtrsim 10^{12}L_{\odot}$. The difference in extinction in the mid-infrared between type-1 and type-2 objects is probably at most a factor of ≈ 3 (see discussion in Section 6). Thus we are able to select very comparable objects with both normal type-1 and obscured quasar

natures in the rest-frame optical.

We defined a “statistical survey” with 90% complete redshift information in order to allow for the inevitable bias towards type-1 objects in our spectroscopic survey. Members of this survey were identified by ordering each sample contributing to the survey in $24\mu\text{m}$ flux density high to low and including objects in the statistical survey by working down the list until the spectroscopic completeness fell below 90% (if at all). This sample consists of 662 objects, with 122 normal type-1s, 86 reddened type-1s, 271 type-2s and 118 “non-AGN”. 23 objects were stars and 42 objects lacked redshifts. Obscured AGN thus dominate the population over the redshift and luminosity range probed by this survey. We will use this survey to discuss the demographics and evolution of these objects in a future paper (Ridgway et al. 2013).

The composite spectrum of the type-2 quasars shows high ionization narrow lines, but is different in the ultraviolet to radio galaxies, with weaker $Ly\alpha$ and other low-ionization species. The [OIII]5007 line emission of our objects correlates well with their $24\mu\text{m}$ luminosity, and both type-1 and type-2 objects lie on the same correlation, showing that mid-infrared selection is indeed capable of selecting type-1 and type-2 quasars with similar intrinsic properties, with no apparent strong dependence of dust covering factor on AGN luminosity.

A significant fraction (259/785, or 33%) of our AGN candidates contained no evidence for an AGN in terms of emission line diagnostics, either because the emission lines were detected, but did not have AGN-like line ratios, or because the spectra had at most only a single weak emission line. 25 of these have some other evidence for AGN (X-ray emission or AGN-related radio emission), an X-ray detection rate not much lower than the type-2 quasars. Overall, the composite spectrum

shows that the stellar population of their host galaxies seems similar to those of the type-2 quasars. Most of them may therefore be AGN whose narrow-line regions are obscured, but as we cannot prove this (except in $\approx 10\%$ of cases where we have other diagnostics) they are excluded from our AGN statistics.

This study reinforces the need for multiple AGN diagnostics to be employed to complete a census of AGN, even for surveys of luminous AGN and quasars such as this one. Nevertheless, our sample will provide important insights into the luminosity dependence and cosmic evolution of obscuration. The publication of the WISE (Wright et al. 2010) all-sky survey will also allow us to continue this survey into even brighter regimes, which will be particularly useful in understanding the luminosity dependence of obscuration at $z < 1$.

NS is the recipient of an Australian Research Council Future Fellowship. ML, AP and TU were visiting astronomers at the Infrared Telescope Facility, which is operated by the University of Hawaii under cooperative agreement no. NNX-08AE38A with the National Aeronautics and Space Administration (NASA), Science Mission Directorate, Planetary Astronomy Program. The Gemini Observatory is operated by the Association of Universities for Research in Astronomy, Inc, under a cooperative agreement with the National Science Foundation on behalf of the Gemini Partnership. Partly based on observations obtained at the Southern Astrophysical Research (SOAR) telescope, which is a joint project of the Ministério da Ciência, Tecnologia, e Inovação (MCTI) da República Federativa do Brasil, the U.S. National Optical Astronomy Observatory (NOAO), the University of North Carolina at Chapel Hill (UNC), and Michigan State University (MSU). We thank the Telescope System Instrumentation Program (TSIP), administered by NOAO, for

the opportunity to observe on the Multiple Mirror Telescope (MMT). This research has made use of the NASA/IPAC Extragalactic Database (NED), which is operated by the Jet Propulsion Laboratory, California Institute of Technology, under contract with the National Aeronautics and Space Administration. This research has made use of data obtained from the *Chandra* Source Catalog, provided by the *Chandra* X-ray center (CXC) as part of the *Chandra* Science Archive. The NRAO is a facility of the National Science Foundation operated under cooperative agreement by Associated Universities, Inc. This paper is dedicated to the late Steve Rawlings, whose work on radio galaxy samples directly inspired the approach taken to this project.

REFERENCES

- Abazajian, K.N., Adelman-McCarthy, J.K., Agüeros, M.A. et al. 2009, ApJS, 182, 543
- Appleton, P.N., Fadda, D.T., Marleau, F.R. et al. 2004, ApJS, 154, 147
- Berta, S., Rubele, S., Franceschini, A. et al. 2006, A&A, 451, 881
- Bertin, E. & Arnouts, S. 1996, A&AS, 117, 393
- Brightman, M. & Nandra, K. (2011), MNRAS, 414, 3084
- Brown, M.J.I., Brand, K., Dey, A. et al. ApJ, 638, 88
- Burgers, A.M. & Hunstead, R.W. 2006, AJ, 131, 114
- Canalizo, G. & Stockton, A. 2000, AJ, 120, 1750
- Ciliegi, P., McMahon, R.G., Miley, G.K. et al. 1999, MNRAS, 302, 222
- Colless, M.M., Dalton, G., Maddox, S. et al. 2001 MNRAS, 328, 1039

- Cleary, K., Lawrence, C.R., Marshall, J.A., Hao, L. & Meier, D. 2007, *ApJ*, 660, 117
- Condon, J.J., Cotton, W.D., Yin, Q.F. et al. 2003, *AJ*, 125, 2411
- Coppin, K., Pope, A., Menéndez-Delmestre, K., Alexander, D.M. & Dunlop, J. 2010, *ApJ*, 713, 503
- Cutri, R.M., Nelson, B.O., Francis P.J. & Smith, P.S. 2002, *IAU Colloq. 184: AGN Surveys*, 284, 127
- Dennefeld, M., Lagache, G., Mei, S. et al. 2005, *A&A*, 440, 5
- de Vaucouleurs, G., de Vaucouleurs, A., Corwin, H.G., Buta, R.J., Paturel, G. & Fouque, P. 1991. *Third Reference Catalog of Bright Galaxies*.
- di Serego-Alighieri, S., Danziger, I.J., Morganti, R. & Tadhunter, C.N. 1994, *MNRAS*, 269, 998
- Donley, J.L., Rieke, G.H., Rigby, J.R. & Pérez-González, P.G. 2005, *ApJ*, 634, 169
- Donley, J.L., Koekemoer, A.M., Brusa, M. et al. 2012, *ApJ*, 748, 142
- Drouart, G., de Breuck, C., Vernet, J. et al. 2012, *A&A*, 548, 45
- Evans, I.N., Primini, F.A., Glotfelty, K.J. et al. 2010, *ApJS*, 189, 37
- Fadda, D., Marleau, F.R., Storrie-Lombardi, L.J. et al. 2006 *AJ*, 131, 2859
- Glikman, E., Gregg, M.D., Lacy, M., Helfand, D.J., Becker, R.H. & White, R.L. 2004, *ApJ*, 607, 60
- Glikman, E., Helfand, D.J., White, R.L., Becker, R.H., Gregg, M.D., Lacy, M. 2007, *ApJ*, 667, 673
- Glikman, E., Urrutia, T., Lacy, M. et al. 2012, *ApJ*, 757, 51
- Gregg, M.D., Lacy, M., White, R.L. et al. 2002, *ApJ*, 564, 133
- González-Solares, E.A., Irwin, M., McMahon, R.G. et al. 2011, *MNRAS*, 416, 927
- Gwyn, S.D.J. 2012, *AJ*, 143, 38
- Haas, M. Willner, S.P., Heymann, F. et al. 2008, *ApJ*, 688, 122
- Herter, T.L. et al. 2008, *Proc. SPIE*, 7014, 30
- Ibar, E. et al. 2009, *MNRAS*, 397, 281
- Jarvis, M., Bonfield, D.G., Bruce, V.A. et al. 2013, *MNRAS*, 428, 1281
- Johansson, P.H., Väisänen, P. & Vaccari, M. 2004, *A&A*, 427, 795
- Jones, D.H., Read, M.A., Saunders, W. et al. 2009, *MNRAS*, 399, 683
- Kewley, L.J., Groves, B. Kauffmann, G. & Heckman, T. 2006, *MNRAS*, 372, 961
- Kimball, A.E., Kellerman, K.I., Condon, J.J. et al. 2011, *ApJ*, 739, L29
- Kocevski, D.D., Lubin, L.M., Lemaux, B.C. et al. 2012, *ApJ*, 744, 148
- Lacy, M., Gregg, M.D., Becker, R.H., White, R.L., Glikman, E., Helfand, D., & Winn, J.N. 2002, *AJ*, 123, 2925
- Lacy, M., Storrie-Lombardi, L.J., Sajina, A. et al. 2004, *ApJS*, 154, 166
- Lacy, M., Wilson, G., Masci, F. et al. 2005, *ApJS*, 161, 41
- Lacy, M., Petric, A.O., Sajina, A. et al. 2007a, *AJ*, 133, 186 (L07)
- Lacy, M., Sajina, A., Petric, A.O. et al. 2007b, *ApJ*, 669, L61

- Lacy, M., Petric, A.O., Martínez-Sansigre, A. et al. 2011, *AJ*, 142, 196
- Lacy, M., Sajina, A., Petric, A.O. et al. 2012, *IAU Symposium*, 284, 224
- La Franca, F., Gruppioni, C., Matute, I. et al. 2004, *AJ*, 127, 3075
- Lanzuisi, G., Piconcelli, E., Fiore F. et al. 2009, *A&A*, 498, 67
- Lawrence, A. 1991, *MNRAS*, 248, 91
- Lawrence, A., Warren, S.J., Almaini, O. et al. 2007, *MNRAS*, 379, 1599
- Leighly, K.M., Dietrich, M. & Barber, S. 2011, *ApJ*, 728, L94
- Lonsdale, C.J., Smith, H.E., Rowan-Robinson, M. et al. 2003, *PASP*, 115, 897
- Liu, G., Zakamska, N., Greene, J.E. 2013, *MNRAS*, tmp 754
- Lusso, E., Hennawi, J.F., Comastri, A. et al. *ApJ*, submitted
- Maddox, S.J., Sutherland, W.J., Efstathiou, G. & Loveday J. 1990, *MNRAS*, 243, 692
- Magliocchetti, M., Maddox, S.J., Wall, J.V., Benn C.R. & Cotter, G. 2000, *MNRAS*, 318, 1047
- Mao, M., Sharp, R., Norris, R.P. et al. 2012, *MNRAS*, 426, 3334
- Manners, J.C., Serjeant, S., Bottinelli, S. et al. 2004, *MNRAS*, 355, 97
- Marleau, F., Fadda, D., Appleton, P.N., Noriega-Crespo, A., Im, M. & Clancy, D. 2007, *ApJ*, 663, 218
- Martínez-Sansigre, A., Rawlings, S., Lacy, M. et al. 2005, *Nat*, 436, 666
- Martínez-Sansigre, A., Rawlings, S., Lacy, M. et al. 2006, *MNRAS*, 370, 1479
- Martínez-Sansgire, A. & Taylor, A.M. 2009, *ApJ*, 692, 964
- McCarthy, P.J. 1993, *ARA&A*, 31, 639
- Middelberg, E., Norris, R.P., Cornwell, T.J. et al. 2008, *AJ*, 135, 1276
- Morel, T., Efstathiou, A., Serjeant, S. et al. 2001, *MNRAS*, 327, 1187
- Norman, C., Hasinger, G., Giacomoni, R. et al. 2002, *ApJ*, 571, 218
- Norris, R.P., Afonso, J., Appleton, P.N. et al. 2006, *AJ*, 132, 2409
- Ogle, P., Whysong, D. & Antonucci, R. 2006, *ApJ*, 647, 161
- Oyabu, S., Ynun, M.S., Murayama, T. et al. 2005, *AJ*, 130, 2019
- Papovich, C., Cool, R., Eisenstein, D. et al. 2006, *AJ*, 132, 231 (P06)
- Park, S.Q., Barmby, P., Fazio, G.G. et al. 2008, *ApJ*, 678, 744
- Polletta, M., Omont, A., Berta, S. et al. 2008, *A&A*, 492, 81
- Rayner, J.T., Toomey, D.W. & Onaka, P.M. et al. 2003, *PASP*, 115, 362
- Reyes, R., Zakamska, N.L., Strauss, M.A. et al. 2008, *AJ*, 126, 2373
- Richards, G.T. et al. 2003, *AJ*, 166, 1131
- Richards, G.T. et al. 2006, *ApJS*, 126, 1131
- Rose, M., Tadhunter, C.N., Holt, J., Ramos Almeida, C, Littlefair, S.P. 2011, *MNRAS*, 414, 3360

- Roseboom, I.G., Lawrence, A., Elvis, M., Petty, S., Shen, Y. & Hao, H. 2012, MNRAS,
- Rowan-Robinson, R. et al. 2005, AJ, 129, 1183
- Sanders, D.B. et al. 2007, ApJS, 172, 86
- Sajina, A., Lacy, M. & Scott, D. 2005, ApJ, 621, 256
- Schechtman, S.A., Landy, S.D., Oemler, A. et al. 1996, ApJ, 470, 172
- Schmidt, M. et al. 1998, A&A, 329, 495
- Serjeant, S. et al. 2001, MNRAS, 322, 262
- Sharp, R.G. Sabbey, C.N., Vivas, A.K., Oemler, A., McMahon, R.G., Hodgekin, S.T. & Coppi, P.S. 2002, MNRAS, 337, 1153 (Sh02)
- Severgnini, P. et al. 2003, A&A, 406, 483
- Shapley, A.E., Steidel, C.C., Pettini, M., Adelberger, K.L. 2003, ApJ, 588, 65
- Simpson, C. et al. 2006, MNRAS, 372, 741 (S06)
- Simpson, C. et al. 2012, MNRAS, 421, 3060 (S12)
- Soltan, A. 1982, MNRAS, 200, 115
- Spinrad, H., Djorgovski, S., Marr, J. & Aguilar, L. 1985, PASP, 97, 932
- Stern, D. et al. 2005, ApJ, 631, 163
- Sopp, H.M. & Alexander, P. 1991, MNRAS, 251, 14
- Strutskie, M.F., Cutri, R.M., Stiening, R. et al. AJ, 131, 1163
- Sturm, E. et al. 2006, ApJ, 653, L13
- Teng, S.H., Wilson, A.S., Veilleux, S., Young, A.J., Sanders, D.B. & Nagar, N.M. 2005, ApJ, 633, 664
- Treister, E., Schawinski, K., Urry, C.M. & Simmons B.D. 2012, ApJ, 758, L39
- Trump, J.R. et al. 2007, ApJS, 172, 383
- Urrutia, T., Lacy, M., Becker, R.H. 2008, ApJ, 674, 80
- Urrutia, T., Becker, R.H., White, R.L., Glikman, E., Lacy, M., Hodge, J. & Gregg, M.D. 2009, ApJ, 698, 1095
- Urrutia, T., Lacy, M., Spoon, H., Becker, R.H., Glikman, E., Petric, A. & Schulz, B. 2012, ApJ, 757, 125
- Watson, M.G. et al. 2009, A&A, 493, 339
- Webster, R.L., Francis, P.J., Peterson, B.A., Drinkwater, M.L. & Masci, F.J. 1998, Nat, 375, 469
- White, R.L. et al. 2000, ApJS, 126, 133
- White, R.L., Helfand, D.J., Becker, R.H. et al. 2007, ApJ, 654, 99
- Whiting, M.T., Webster, R.L. & Francis P.J. 2001, MNRAS, 323, 718
- Wisotzki, L., Cristlieb, N., Bade, N., Beckman, V., Koehler, T., Vanelle, C., Reimers, D. 2000, A&A, 358, 77
- Yan. L. et al. 2007, ApJ, 658, 778
- Zakamska, N.L. et al. 2003, AJ, 126, 2125

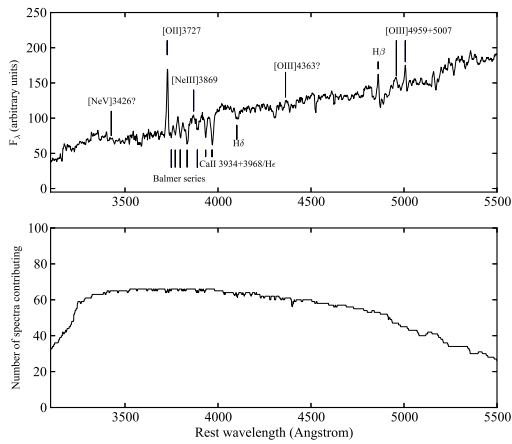


Fig. 14.— The composite spectrum of objects lacking AGN signatures in their individual spectra. The bottom panel shows the number of spectra contributing at each wavelength.

A. Notes on individual objects

A.1. SW021749.00-052306.9

This object had a redshift of 0.987 assigned by L07 on the basis of the detection of a single emission line, presumed to be [OII]3727. Lanzuisi et al. (2009) obtained an improved spectrum of this object, showing that the redshift is in fact 0.914 (consistent with the line we identified in L07 being [NeIII]3869 rather than [OII]). Lanzuisi et al. also detect strong [OIII]5007 emission beyond the wavelength range of our original spectrum, confirming it as a type-2 AGN.

A.2. SW021928.77-045433.7

There is a clear detection of an emission line in the H -band spectrum from Gemini, but other features are less certain. The [NeV]3426 line is in a region of poor atmospheric transmission, so may be a noise spike. The optical spectrum, however, shows marginal evidence of a spectral break around the wavelength of $\text{Ly}\alpha$ if the redshift is 3.23, and a marginally significant feature corresponding CIV1549 if the line in H -band being [OII]3727. We therefore assign this object a redshift of 3.23 with a redshift quality of two.

A.3. SW021822.13-050614.1

This low redshift ($z = 0.044$) object is an X-ray source. Optically it is classed as a non-AGN, but, as discussed by Severgnini et al. (2003), its true nature is an AGN.

A.4. SW021947.53-051008.5

This quasar shows a blueshifted HeI line in absorption (Figure 3). Leighly, Dietrich & Barber (2011) discuss a broad absorption line quasar with HeI absorption that may be similar to our object.

A.5. SW022003.58-045145.6

This object is a highly dust-reddened quasar at $z = 1.33$ (Figure 3). The Hale and Gemini near-infrared spectra show only a single broad emission line at $1.53\mu\text{m}$, however, a Keck/LRIS spectrum shows several UV emission lines at a redshift of $z = 1.33$.

A.6. SW104159.83+585856.4

This otherwise unremarkable $z = 0.342$ type-2 quasar has an anomalous emission line at 4331\AA which may correspond to an emission line from a higher redshift galaxy lensed by the quasar.

A.7. SW105201.92+574051.5

This object was independently identified by Coppin et al. (2010) as a high redshift, submm bright obscured quasar (AzLOCK.01 in that paper). The *Spitzer* IRS spectrum obtained by Coppin et al. shows both strong PAH features and a strong continuum at $z \approx 2.5$. Our Gemini/NIRI spectrum (Figure 4) shows a narrow $\text{H}\alpha$ emission line at $z = 2.467$.

A.8. XFLS 171053.51+594433.1

This object, the second-highest redshift quasar in the sample, was first identified by Marleau et al. (2007) in a survey of radio emitters in the XFLS. The quasar has a flux density of 2.4mJy at 1.4GHz, so is radio-intermediate in nature. The optical spectrum in figure 3 of Marleau et al. shows only narrow Ly α and NV1240, but our Hale spectrum with Triplespec (Figure 6) clearly shows a broad H β emission line, hence its classification as a reddened type-1 quasar.

A.9. XFLS171419.9+602724

This object, a $z = 2.99$ type-2 quasar is discussed in detail in Lacy et al. (2011).

A.10. XFLS171754.6+600913

At $z = 4.27$, this is the highest redshift object in our sample, and the most luminous. It is a dust-reddened type-1 quasar with a mini-LoBAL system (Figure 6) with an overall luminosity of $\approx 10^{14}L_{\odot}$, and is a *Chandra* X-ray detection, though falling well below the X-ray – 15 μ m luminosity correlation, presumably due to absorption.